Journal Pre-proof

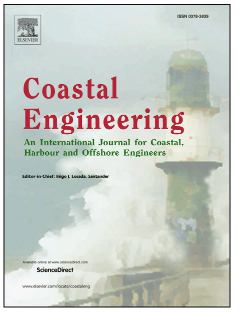

Wave and structure interaction using multi-domain couplings for Navier-Stokes solvers in OpenFOAM®. Part I: Implementation and validation

Benedetto Di Paolo, Javier L. Lara, Gabriel Barajas, Íñigo J. Losada

PII: S0378-3839(20)30485-3

DOI: https://doi.org/10.1016/j.coastaleng.2020.103799

Reference: CENG 103799

To appear in: *Coastal Engineering*

Received Date: 25 March 2020

Revised Date: 30 September 2020

Accepted Date: 10 October 2020

Wave and structure interaction using multi-domain couplings for Navier-Stokes solvers in OpenFOAM®. Part I: Implementation and validation

Benedetto Di Paolo[a,*], Javier L. Lara[a], Gabriel Barajas[a], Íñigo J. Losada[a]

[a]*IHCantabria - Instituto de Hidráulica Ambiental de la Universidad de Cantabria*
C/Isabel Torres n° 15, Parque Científico y Tecnológico de Cantabria, 39011 Santander, Spain.

Abstract

This paper and its companion (Di Paolo et al. (b), submitted) present near-far field coupling schemes of Navier-Stokes (NS) equations for high-fidelity numerical modelling of wave generation, transformation and interaction with structures. The computational domain is subdivided into near and far field zones (2D and 3D subdomains, respectively) in which the NS equations are solved adopting the Finite Volume Method. The couplings can be made through the one-way or two-way exchange of flow information, thus providing a complete tool for studying one or bi-directional processes in which the three-dimensional flow is expected to be confined in the near field. The global coupled system, which is built on the OpenFOAM® platform, is based on a multi-domain approach in which the sub-domains (i.e., 2D and 3D meshes) are built independently.

In Part I, the coupling methodologies have been validated against full 3D models taking into account wave propagation under different conditions with excellent results and high efficiency.

Part 2 (Di Paolo et al. (b), submitted) involves the validation and application of the proposed methodologies to complex wave-structure interaction studies.

Keywords: Coupled models, Navier-Stokes, One-way, Two-way, OpenFOAM, 2D-3D

1 Introduction

During the past decades, the use of Computational Fluid Dynamics (CFD) based models has experienced an important increase in coastal and offshore engineering as they are highly accurate to study wave transformation, wave-breaking and fluid-structure interaction processes. Because the computational cost is tremendously high when using a single 3D model, its application is unfeasible for large domains (Vandebeek et al. (2018)). Therefore, traditionally the application of CFD modelling has been limited to small scale domains forced by appropriate boundary conditions. However, the main drawback of this approach is that it does not allow to properly include wave propagation and shoaling. Thus, in recent years, a considerable research effort has been made on developing near-far field coupled models that were able to deal with the above issue in an efficient way (e.g. Altomare et al. (2014), Vandebeek et al. (2018)).

*Corresponding author
Email addresses: benedetto.dipaolo@unican.es (Benedetto Di Paolo), jav.lopez@unican.es (Javier L. Lara), gabriel.barajas@unican.es (Gabriel Barajas), inigo.losada@unican.es (Íñigo J. Losada)

Coupled models for water wave applications have been generally classified based on the physics involved, i.e. single or multi physics, and, depending on the linkage between solvers, as ”one-way” or ”two-way”. One-way couplings, also known as ”weak” or ”one-directional” couplings allow information to pass in one direction, while ”two-way” coupling, also known as ”strong” or ”bi-directional” couplings allow information to be exchanged in two directions. ”One-way” couplings are used when the processes involved can be assumed to be one-directional whereas ”two-way” couplings are required when the bi-directionality cannot be neglected.

In the following, some previous works, considered key for the development of the current research, are reviewed and ranked from computationally cheaper or ”lower” to expensive or ”higher” models. Here we focused on the coupled models (considering single or multi physics) addressing the hydrodynamics of water waves. Considering the governing equation solved four categories can be identified, i.e., fully non-linear potential flow (FNPF), non-linear shallow water (NLSW), Boussinesq-type (BT) and Navier-Stokes based (CFD) models. The coupling techniques among the above, in ”one-way” or ”two-way” modes, are reviewed in the following.

Several weak (”one-way”) coupled models (Lagrangian or Eulerian) have been developed by the scientific community. For example, fully non-linear potential solvers (FNPF) have been coupled with RANS-VOF and Smoothed Particle Hydrodynamics (SPH) models (e.g. Hildebrandt et al. (2013), Fourtakas et al. (2018), respectively). Hildebrandt et al. (2013) simulated wave impact on a tripod structure by implementing a one-way coupling as no reflection of the impact waves was expected. Fourtakas et al. (2018) validated the FNPF-SPH coupling for the propagation of two sinusoidal waves but the method was not tested for wave interaction, neither with coastal nor with offshore structures. The one-directional coupling methodology has been applied to link BEM (Boundary Element Method) potential flow codes and VOF solvers (e.g. Lachaume et al. (2003), Biausser et al. (2004)). In particular, Lachaume et al. (2003) modelled breaking and post-breaking waves on slopes by coupling BEM and RANS-VOF software. Zhang et al. (2013) coupled Navier-Stokes (NS) with Potential Flow (PF) solvers for near and far field wave propagation, respectively, describing weak and strong coupling implementation. Duz et al. (2016) implemented a coupling between OceanWave3D (FNPF) and ReFRESCO (RANS-VOF) models. They analysed the capabilities of two FNPFs and SWASH (NLSW) models and stated that none of them is superior to the other for wave propagation studies, thus the computationally cheapest one (OceanWave3D) was coupled with the RANS-VOF solver. Paulsen et al. (2014) also presented a one-way coupling between the potential flow solver OceanWave3D and a RANS-VOF solver in OpenFOAM environment. The one-way coupled method was validated for wave interaction with surface piercing structures, also considering complex hydrodynamics (i.e. multi-directional irregular waves on a sloping bed). Another interesting work was proposed by Vukčević et al. (2016) . They implemented a decomposition method in which a generic field is decomposed into an incident wave forcing component and a perturbation component. The incident wave forcing component was obtained from a potential flow model, while the perturbation component was adjusted in order to satisfy the conservation equations in the NS based model. The method implemented by Vukčević et al. (2016) has been recently reproposed by Li et al. (2020). The main differences of their work lie in the simplification of continuity and momentum equations, the use of VOF technique instead of the Decomposed Level-Set approach and the interpolation method used to transfer information from the potential solver to the NS model. The latter showed that the Decomposed Level-Set approach has no advantages against the VOF method.

NLSW codes have been coupled with RANS/VOF solvers (Vandebeek et al. (2018)). Vandebeek et al. (2018) validated a weak coupling between the non-hydrostatic NLSW model (SWASH) and the RANS-VOF (OpenFOAM). However, the coupling was only tested for the propagation of a first order linear wave on a flat bottom. Neither wave structure interaction (WSI) nor coupling effects were analysed. The results of regular wave propagation showed a small damping in the free surface elevation far from the coupling zone. SWASH has also been "one-way" coupled with SPH as proposed by Altomare et al. (2014) for coastal engineering problems. They motivated their work based on the fact that SWASH is able to propagate waves with comparable accuracy to BT models while the full SPH simulation could damp waves if applied to long distances. However SWASH may lead to computation stability problems when applied to rapidly changing bathymetry or structures (Altomare et al. (2014)).

Boussinesq-type models (BT) have found favour over the past decades as they are a good compromise between physical adequacy and computational demand, thus becoming probably the best alternative to CFD codes (Brocchini (2013)). BT models have been coupled with Eulerian and Lagrangian CFD codes. Kassiotis et al. (2011)) proposed the coupling between SPH and BT models. They concluded that the weak coupling was only accurate when waves did not reflect from SPH to the BT domain (Kassiotis et al. (2011)). However, a discontinuous and non-smooth velocity profile appeared at the interface when passing information from an empty flume in the BT domain to the SPH region, before reflection took place (see Figure 4 of Kassiotis et al. (2011)).

Some works can be found regarding CFD-CFD couplings in one-way mode. Kumar et al. (2015) coupled, breaking waves on 3D structures SPH-FVM solvers within the OpenFOAM® environment. They used the FVM solver from OpenFOAM to simulate a large domain while the application of SPH was limited to a small region on free surfaces and near deformable boundaries. El Safti et al. (2014) coupled 2D with 3D RANS-VOF simulations in OpenFOAM® by forcing the 3D model by means of post-processed sensor data in the 2D simulation. In the work of El Safti et al. (2014) neither active wave absorption (AWA) nor a fully coupled multi-region scheme were considered, so that although a 2D-3D coupling was developed the domains were increased at the interfaces as the relaxation method (Jacobsen et al. (2012)) was used (two relaxation zones). Furthermore, in the work presented in El Safti et al. (2014), Large Eddy simulation was performed which considerably increased the computational time, making the methodology unfeasible for the study of large domains. In addition, no two-way coupled scheme was applied to the 2D-3D coupling.

Many past works have also focused on ”two-way” methodologies to analyse those cases where the flows travel through the distinct domains in different directions. Verbrugghe et al. (2018) and Verbrugghe et al. (2019) proposed strong FNPF-SPH couplings. In Verbrugghe et al. (2018) the communication between models was implemented using OpenMPI, that was managed through a main script coded in Python language. Although, different non-linear waves were propagated and some simulation for WSI were performed, neither shallow foreshores (coastal applications) nor three-dimensional local effects were considered. Recently, Kemper et al. (2019) implemented a new nested two-way coupling between FNPF and RANS-VOF models to study hydrodynamics around WEC arrays. The coupled model presented by Kemper et al. (2019) was successfully validated against experimental and analytical solutions. However, the authors stated as the main limitation of the approach that the model was not able to run in parallel and pointed out the need for filtering the RANS-VOF free surface signal before using it as a boundary condition for the FNPF solver. Sriram et al. (2014) carried out a unique 2D-2D strong-coupling between the Improved Meshless Local Petrov Galerkin method (IMLPG_R) based on NS equations and a finite element method model (FEM) based on FNPF. Some research has also addressed the coupling of BEM-based models with potential models and Level-Set (LS) or VOF solvers (e.g. Colicchio et al. (2006) and Kim et al. (2010), Guo et al. (2012), respectively). Another interesting coupling between FNPF and RANS models was implemented in OpenFOAM by Lu et al. (2017). They used an overlapping domain for developing a near-far field method for WSI including overset mesh capabilities in the RANS solver. Janssen et al. (2010) formulated a strongly coupled model linking FNPF and Lattice-Boltzmann based solvers in order to study wave breaking and wave structure interaction. Mintgen and Manhart (2018) implemented a bi-directional coupling of the 2D shallow water equations (SWE) and the 3D RANS-VOF model. An innovative multi-region approach in OpenFOAM was used to combine both methods, and the communication between them was achieved via boundary conditions following a Dirichlet-Neumann approach (see Tables 1 and 2 of Mintgen and Manhart (2018)). However, this work is of limited applications in coastal engineering as only shallow water flows can be studied in the far field. A BT-SPH two-way coupling was presented by Narayanaswamy (2008), in which FUNWAVE (BT) and SPHysics (SPH) were linked in order to study wave propagation. Sitanggang (2008), Sitanggang and Lynett (2010) and Sitanggang et al. (2007) presented a linkage between a 1D horizontal BT solver and a 2DV RANS-VOF model for large-scale simulation. They implemented a nested technique to couple both models. Validation was presented for wave propagation, wave overtopping, wave interaction with permeable structures and large-scale tsunami wave simulation. Despite of very good results obtained by these authors, the coupled methodology was limited to study 2D problems as the RANS-VOF model did not include 3D solutions of the NS equations.

Finally, one of the most interesting two-way couplings was proposed by Ferrer et al. (2016), in which a multi-region compressible-incompressible scheme (multi-physics) was implemented in the OpenFOAM® framework to deal with aerated impact in numerical wave tanks. It is worth noticing that the multi-region approach means that different finite volume meshes are built, each one containing a specific solver, and are solved in a unique global simulation. On the other hand, in a "partitioned approach" different pieces of software (solvers) are independently used, and the interface among them is in charge of the message passing information (MPI etc.), as shown in Verbrugghe et al. (2018). Table 1 summarises the references above and also includes other interesting works.

In this work, new coupling methodologies are developed in order to study wave propagation, breaking and interaction with structures using CFD based models only. Coupling 2D and 3D CFD solvers can represent an extremely accurate and efficient approach as it is a compromise between the computational cheaper couplings (e.g. NLSW-CFD or BT-CFD) and the extremely expensive full 3D simulations. A key aspect of the proposed research is that by using the 2D-3D RANS-RANS approach, the flow variables of the 3D model are continuously enriched by means of highly resolved hydrodynamics from the 2D solver, thus increasing the accuracy of the near-far field hydrodynamic modelling.

Although the use of BT or non-hydrostatic NLSW codes for wave transformation has been common practise, the application of CFD allows to reduce uncertainties in hydrodynamic modelling as the full set of NS equations is solved. Moreover, the performance of heterogeneous couplings (different models, e.g. NLSW-CFD or BT-CFD) has not been analysed in depth considering an extended range of wave forcings, local conditions (i.e. shallow, deep and intermediate waters) and the influence of depth varying flow at the coupling zone. Difficulties may also arise in order to avoid wave damping and distortion when matching "heterogeneous models" at the coupling zone. Such as, in BT-CFD couplings the BT model can only provide velocity and free surface at a reference depth (Narayanaswamy (2008)). This leads to a loss of accuracy especially when the velocity profile varies significantly along the water depth. Moreover, an overlapping zone is generally needed to develop BT-CFD couplings (Narayanaswamy (2008), Sitanggang and Lynett (2010), Kassiotis et al. (2011)). For complex cases, where the 3D domain typically governs the computational time, the BT-CFD model might be more expensive than a 2D-3D CFD-CFD one.

The methodology developed in the present work aims at providing an extremely accurate tool to model numerically those processes in which three dimensional flows are dominating in the near-field. The computational speed-up that can be achieved with a 2D-3D approach is high compared to the fully 3D modelling. In fact, the 2D-3D based coupling is further justified by the fact than the CPU time is generally governed by the 3D model whereas the 2D approach is computationally cheaper. Moreover, the accuracy in wave generation is much higher when using a CFD model as the spatial variability of the wave profiles can be estimated with great precision. As an example, the mimicking of wave-maker devices is a unique asset of CFD solvers compared to the computationally cheaper codes. Finally, an additional advantage of a RANS-RANS coupled approach is that it allows forcing the position of the coupling zone closer to the breaking point, while the application of other models (e.g. BT or NLSW) restricts the definition of the coupling boundary to far from the breaking conditions.

The coupled models presented in the current work are intended: **(i)** to accurately simulate first and second order waves, the propagation and shoaling processes from far to near field from far to near field, also considering the interaction with complex bathymetry or submerged structures, **(ii)** to provide a complementary tool of one-way and two-way couplings to be used depending on flow characteristics, **(iii)** to simulate wave transformation over larger domains with a reduced computational time and **(iv)** to develop an easy-to-use and parallelised multi-domain scheme in which each computational mesh is built independently. The coupled models presented are capable of simulating large domains in standard desktop computer in a very efficient way, increasing the range of application and the use of CFD to real cases.

The paper is organised as follows. Section 2 describes the coupling methodology developed for the one-way and two-way approaches. Then, Section 3 illustrates the validation of the methodology. Section 4 discusses the advantages of the coupled models and concluding remarks close the paper.

Authors	Models	Fields transf.	Fields adjusted	wave refl. technique	Transfer type	Direction	DD	Simulation
Hildebrandt et al. (2013)	**FNPF-CFD**	$\mathbf{U}$		-	BCs	One-way	decoupled	parallel
Lachaume et al. (2003)	"	$\mathbf{U}$, p		-	BCs & overlap	One-way	decoupled	parallel
						Two-Way	coupled	parallel
Biausser et al. (2004)	"	ζ, $\mathbf{U}$, p		-	cell-centres	One-way	decoupled	-
Duz et al. (2016)	"	ζ, $\mathbf{U}$		-	BCs	One-way	decoupled	parallel (CFD only)
Vukčević et al. (2016)	"	ζ, $\mathbf{U}$		relaxation zones	cell-centres	One-way	decoupled	parallel
Li et al. (2020)	"	ζ, $\mathbf{U}$		relaxation zones	cell-centres	One-way	decoupled	parallel
Paulsen et al. (2014)	"	ζ, $\mathbf{U}$		relaxation zones	BCs	One-way	decoupled	parallel
Colicchio et al. (2006)	"	ζ, $\mathbf{U}$, p		-	overlap	Two-way	coupled	serial
Kim et al. (2010)	"	$\mathbf{U}$	ζ (**FNPF**)	sponge layer	overlap	Two-way	coupled	-
Janssen et al. (2010)	"	ζ, $\mathbf{U}$, p		absorbing beach, piston pressure	BCs overlap	One-way Two-way	- coupled	- -
Guo et al. (2012)	"	ζ, $\mathbf{U}$		sponge layer	overlap	Two-way	coupled	-
Sriram et al. (2014)	"	$\mathbf{U}$, p		-	overlap	Two-way	coupled	serial
Lu et al. (2017)	"	$\mathbf{U}$	ζ (overlap)	-	overlap	Two-way	coupled	parallel
Verbrugghe et al. (2018)	"	ζ, U_x	ζ(FNPF)	relaxation zones	overlap	Two-way	coupled	parallel
Verbrugghe et al. (2019)	"	ζ, U_x	ζ(FNPF)	open boundaries	overlap	Two-way	coupled	parallel
Kemper et al. (2019)	"	ζ, $\mathbf{U}$		relaxation zones	overlap	Two-way	coupled	serial
Mintgen and Manhart (2018)	**SWE-CFD**	h, q, ζ, $\mathbf{U}$, p, k, ω		-	BCs	Two-way	coupled	parallel
Altomare et al. (2014)	**NLSW-CFD**	$\mathbf{U}$		-	BCs	One-way	decoupled	parallel
Vandebeek et al. (2018)	"	ζ, $\mathbf{U}$		-	BCs	One-way	coupled	parallel
Kassiotis et al. (2011)	**BT-CFD**	ζ, $\mathbf{U}$		-	BCs & overlap	One-way	decoupled	-
Sitanggang (2008)	"	ζ, $\mathbf{U}$		-	overlap	Two-way	coupled	parallel
Narayanaswamy (2008)	"	ζ, $\mathbf{U}$		-	overlap	Two-way	coupled	-
Kumar et al. (2015)	**CFD-CFD**(3D)	merge of CFD-CFD		-	overlap	One-way	decoupled	parallel
El Safti et al. (2014)	**CFD-CFD**(2D-3D)	ζ, $\mathbf{U}$		relaxation zones	overlap	One-way	decoupled	parallel
Ferrer et al. (2016)	**CFD-CFD**(3D-3D)	ζ, $\mathbf{U}$, p, k, ω		sponge layers	BCs	Two-way	coupled	parallel
Di Paolo et al. (a)	**CFD-CFD**(2D-3D)	ζ, $\mathbf{U}$		active absorption	BCs	One-way	coupled	parallel
Di Paolo et al. (a)	**CFD-CFD**(2D-3D)	ζ, $\mathbf{U}$, p, k, ω		active absorption	BCs	Two-way	coupled	parallel

Table 1: Tabulated overview of the existing coupled models.. ζ, $\mathbf{U}$, p, k and ω are the free surface, velocity, pressure, turbulent kinetic energy and dissipation rate fields, respectively. h, q are the flow-depth and specific discharge field of SWE models. U_x is the horizontal velocity component. BCs stands for boundary conditions, while overlap refers to the use of overlapping zones at the interfaces between the different models and the symbol - is used where no information or specifications are found. DD stands for domain decomposition, which can be coupled if one single simulation is carried out, or decoupled otherwise.

2 The coupling methodology

The present study is based on the decomposition of a global domain into separated 2D and 3D domains that act as partitioned sub-domains in which different local meshes can be defined (e.g. Mintgen and Manhart (2018)). This approach makes it possible to build regions with different spatial dimensions (i.e. 2D/3D), which is a major advantage over a single global mesh approach (e.g.

Ferrer et al. (2016)). The exchange of information between 2D and 3D domains can be performed by means of one-way or two-way coupling algorithms, and the couplings take place via the values of the boundary conditions computed from the flow variables of the neighbour domains.

2.1 Domain partitioning and coupling types

Within the proposed approach, the global domain can be spatially partitioned into several subdomains (2D and 3D), which may or may not overlap to each other. The decomposition method can be classified into three categories: *Dirichlet-Dirichlet* (overlapping subdomains), *Dirichlet-Neumann* (non-overlapping subdomains) and *Neumann-Neumann* (non-overlapping subdomains). The reader may refer to Quarteroni and Valli (1999), Vreugdenhil (2013) and Mintgen and Manhart (2018) for a comprehensive description of the above methods. A Robin-Robin approach is also available for non-overlapping subdomains (Ferrer et al. (2016)). Ferrer et al. (2016)developed boundary conditions based on the specification of values and gradients at the interfaces. By doing so, a mixed type boundary condition (Robin type) is specified. The boundary conditions were deduced from the discretization of the governing equations (transport equations) as will be better described later in this study. In this work, two non-overlapping 2D and 3D sub-domains (Ω_{2D} and Ω_{3D}) are considered. The regions are mutually connected through an interface boundary $\partial\Omega_{2D/3D}$ which allows the exchange of information. Figure 1 shows the scheme of the coupled sub-domains. Once the coupling scheme is defined, i.e. overlapping or non-overlapping sub-domains, the coupling method in the space domain must be chosen. In particular, three options are possible (Sriram et al. (2014)):

1. fixed boundary interface
2. moving boundary interface
3. moving overlapping zone interface

In a RANS-VOF approach, options 2 and 3 result in a high computational cost, as moving grids are needed at the interfaces.

Therefore, in this work a fixed boundary interface is used for coupling the sub-regions, and both one-way and two-way coupling algorithms have been developed. For the one-way scheme the *Dirichlet* boundary conditions have been applied, whereas for the two-way coupling a *Robin-Robin* approach has been used following the approach developed by Ferrer et al. (2016). The coupling methods are described in Sections 2.5 and 2.6.

2.2 Coupling solving in time domain

The quality of the numerical model results is closely related to the Courant number (CFL), which should be less than 1 to ensure that no information is lost when flowing through the computational cells. Thus, the upper limit of the Courant number automatically sets the maximum time step (δt). When coupling different models, the calculated time step in each sub-domain is generally different. However, in order to couple simulations, we need to exchange the information at the same instants of time so as not to alter the physical processes involved. Two approaches are available:

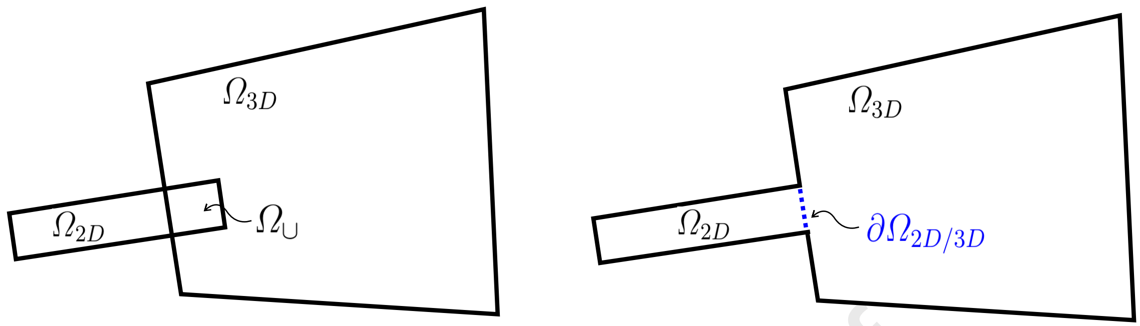

Figure 1: On the left: overlapping sub-domains. On the right: non-overlapping sub-domains (present work).

1. multi time step
2. single time step

The first approach (multi time step) is suitable when coupling a computationally expensive model with another one with a lower computational cost. The time step of the lower computational cost model is usually several orders of magnitude higher than that of the higher computational cost model, such as for example fluid-soil interaction models (Li (2016)). The model with lower computational cost reduces the computational time by not solving each small time step, but only when the following condition is verified:

$$t_i - t_j > \delta t_{ref} \tag{1}$$

where t_i is the actual run-time in which we solve the high computational cost model, t_j is the last run-time we solved the lower computational cost model and δt_{ref} is a ”sampling” time interval in which the low-cost model has to be solved once.
On the other hand, when it comes to numerical models that are comparable in computational time, the second approach (single time step) is reasonable and feasible. The time step derived from each RANS solver is of the same order of magnitude, and as there is a need to ”synchronize” the models at each time step for transferring information, the single time step method is logically used. The time step is calculated as follows:

$$\delta t = min[\delta t_{2D}, \delta t_{3D}] \tag{2}$$

where δt_{2D} and δt_{3D} are the theoretical time steps from the Ω_{2D} and Ω_{3D} sub-regions, respectively. This approach is acceptable as generally the computation of the 2D domain is less computationally expensive than the 3D region. In the literature the same technique has been applied by other researchers for coupling compressible and incompressible RANS solvers (Ferrer et al. (2016)).

2.3 Meshes and interfaces

The proposed methodologies operate within arbitrary polyhedral FV frameworks. Polyhedral meshes have the advantage of adapting well to the bottom configuration and the structure shapes we define inside the computational domains. Each polyhedral cell has a 3D-Cartesian coordinate (x,y,z) associated with its elements, i.e., cell-centre, face-centre and edge-point coordinates.
A 2D-mesh is constructed with one cell in the horizontal direction (y-axis). The 3D-mesh can be defined arbitrarily in terms of the number of elements in the horizontal plane. With regard to interface meshes, some restrictions are introduced. To speed-up the calculation through the boundary conditions in the mutual interfaces, coincident meshes along the vertical direction (z-axis) were used for the proposed models, while 2D and 3D interfaces did not match along the y-direction. In addition, for the one-way coupling the meshes between the sampling sensor (Figure 2 in Section 2.5) and the interfaces match along the z-axis. By doing so, the mapping of information between the different models is faster, as there is no need for an interpolation procedure along the vertical direction which is justified in most of the cases. However, if meshes do not match in the vertical direction at the interface, an additional interpolation procedure is needed. An example of the meshes at the interfaces is shown in Figure 3 (panel a). How the information is transferred is explained later in the paper.

2.4 Governing equations

The RANS-VOF equations are solved in both Ω_{2D} and Ω_{3D} sub-domains. The mass conservation equation reads:

$$\frac{\partial u_i}{\partial x_i} = 0 \tag{3}$$

while the momentum equation is as follows:

$$\frac{\partial \rho u_i}{\partial t} + u_j \frac{\partial \rho u_i}{\partial x_j} = -g_j x_j \frac{\partial \rho}{\partial x_i} - \frac{\partial p^*}{\partial x_i} - f_{\sigma i} - \frac{\partial}{\partial x_j} \mu_{eff} \left(\frac{\partial \rho u_i}{\partial x_j} + \frac{\partial \rho u_j}{\partial x_i} \right) \tag{4}$$

and the Volume of Fluid method (VOF) is used for tracking the free surface (Rusche (2003), Berberović et al. (2009)):

$$\frac{\partial \alpha}{\partial t} + \frac{\partial u_i \alpha}{\partial x_i} + \frac{\partial u_{ci} \alpha (1-\alpha)}{\partial x_i} = 0 \tag{5}$$

where u_i are the ensemble averaged components of the velocity, x_i are the Cartesian coordinates, p^* is the pressure in excess of hydrostatic, g is the acceleration of gravity, ρ the density; x_i is the coordinate and α is the volume fraction (VOF indicator function), which is assumed to be 1 for the water phase and 0 for the air phase. The surface tension $f_{\sigma i}$ is equal to $f_{\sigma i} = \sigma \kappa \frac{\partial \alpha}{\partial x_i}$, where σ is the surface tension constant and κ the curvature (Brackbill et al. (1992)). Finally, μ_{eff} is the efficient dynamic viscosity, which takes into account the molecular (μ) and turbulent viscosity effects ($\rho \nu_t$): $\mu_{eff} = \mu + \rho \nu_t, \nu_t$ is the eddy viscosity, and is provided by the turbulence closure model used. The compression velocity u_{ci} is calculated as $|u_{ci}| = min[c_\alpha |u_i|, max(|u_i|)]$, where by default the compression coefficient c_α is taken to be 1.

The turbulence model proposed by Larsen and Fuhrman (2018) has been introduced in this work as it provides a stable solution for the over production of turbulence levels when dealing with free surface waves. The reader is referred to Larsen and Fuhrman (2018) for descriptions, validations and discussions of the stabilized turbulence models and to Devolder et al. (2017) for the explanation of the buoyancy term, which is similarly introduced into the model of Larsen and Fuhrman (2018). All simulations in Part I have been run in laminar mode. The description of BCs for turbulence quantities were introduced to be used when three-dimensional effects are expected to appear (i.e. Part II).

2.5 The "one-way" coupling procedure

To achieve the one-way coupling between 2D and 3D domains, several boundary conditions (BCs) are required. It is well known that the number and type of boundary to be set for generating water waves depends on the technique used. In this work, we work with generation and active absorption at the interfaces (also known as static and dynamic BCs). As the coupling interfaces are static, in a RANS-VOF scheme condition the velocity field and volume fraction (water level) need to be set (Higuera et al. (2013a)). Velocity profiles are only imposed to the water phase.

The one-way coupled algorithm proposed in this work is based on the transfer of information from a virtual gauge (sampling cells inside the $\varOmega_{2D}$ region in Figure 2) to the 3D patch of the $\varOmega_{2D}$ domain. The virtual gauge (sampling sensor) is located inside the 2D domain at a user-specified distance from the coupled interfaces. All the flow variables can be sampled from the sampling sensor, i.e. VOF indicator function (hereafter α), velocity u_i (hereafter **U**), pressure in excess of hydrostatic p^*, turbulence kinetic energy k, dissipation rate ω and turbulent viscosity ν_T.

To achieve a weak-coupling, the variables α and U have to be transferred, resulting in a "one-way" Dirichlet coupling of these two variables. The two variables are directly transferred from the virtual gauge in the 2D domain, i.e. α and **U**. The way the other field quantities are treated is explained later in the paper. The 2D interface (outlet of the 2D region) and the 3D coupled boundary (inlet of the 3D domain) are defined as $\varGamma_{2D}$ and $\varGamma_{3D}$, respectively.

In the following, the boundary conditions implemented are presented in detail (i.e. for α and **U**). Pressure and turbulent quantities at the 2D-3D interfaces are also described.

2.5.1 Level boundary condition at $\varGamma_{3D}$

The VOF function α at the 3D patch (hereafter $\alpha_{\varGamma_{3D}}$) is set as a Dirichlet boundary condition on $\varGamma_{3D}$, since the flow is only allowed to enter into $\varOmega_{3D}$. In Figure 3, panel a, it is shown how a generic variable ϕ is transferred from a sampling sensor in $\varOmega_{2D}$ to $\varGamma_{3D}$. In particular, as the interfaces match along the z-axis, the variables at the cell centres of sampling cells correspond to the variables at the face centres of the 3D patch. to transfer the information we only need to detect the volume fraction of each cell (submerged, emerged or partially submerged) at the sampling sensor in $\varOmega_{2D}$. Panel b of Figure 3 shows the different type of cells: emerged (α = 0.0), partially submerged (0<α<1, e.g. α = 0.7) and submerged (α = 1.0).

The information collected inside the 2D-region is repeated along the 3D patch width (y-axis). The way this BC works is summarised as follows:

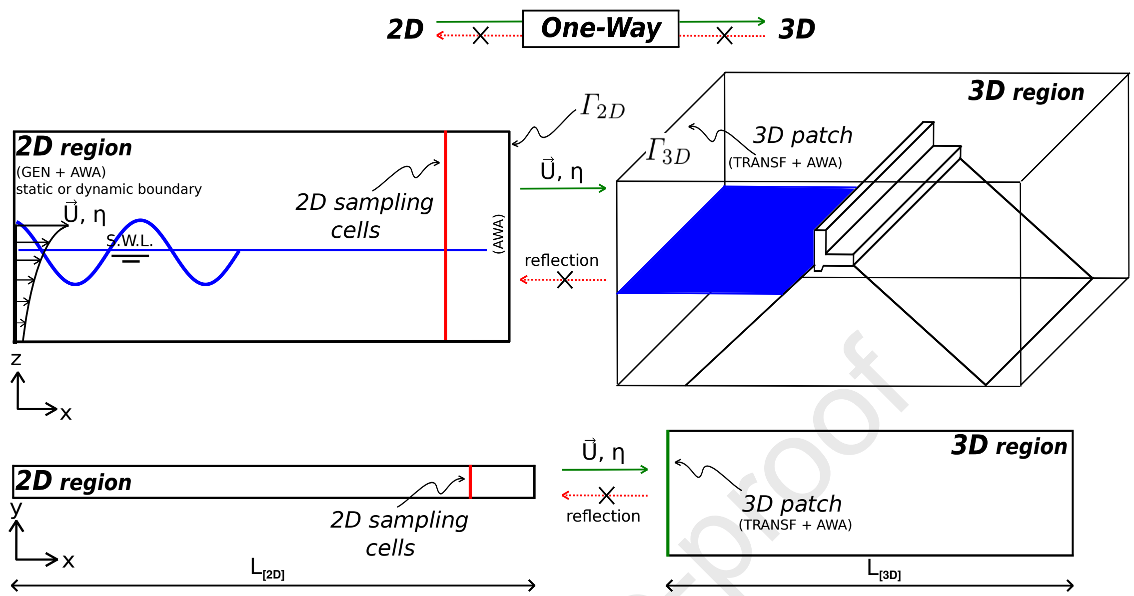

Figure 2: One-way (one-directional or weak) coupling scheme implemented in OpenFOAM® (v1812) framework. "GEN", "AWA" and "TRANSF" stand for wave generation, active wave absorption and transferred information, respectively. Top panel: cross section (x-z). Bottom panel: top view (x-y).

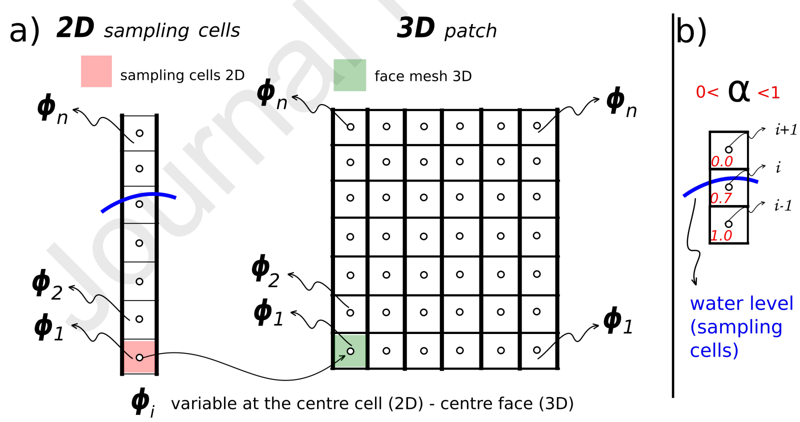

Figure 3: Generic variable (ϕ) transfer procedure for the one-way coupling. On the left the 2D OpenFOAM virtual patch mesh (sampling sensor) is drawn while on the right the 3D patch grid is shown. Panel a): 2D sample cells and 3D patch faces. Panel b): alpha field at the sampling cells.

- *step 1:* Reading the position of the sampling sensor, i.e. coordinate x(m) of the 2D sampling cells in Figure 2
- *step 2:* Searching for the nearest cell centres along the z-axis for the input x(m)
- *step 3:* Collecting the vector with volume fraction values at the cell centres and transferring the information (collected vector) to the 3D interface (matching interfaces, no interpolations are needed). Note that the ratio $\frac{n^o El \Gamma_{3D}}{n^o El \Gamma_{2D}}$ represents the number of faces of the 3D patch in

the y direction (spanwise).

The key steps of the implementation of the above procedure is summarised in Algorithm 1. In the Algorithm 1, $n^o El\Gamma_{2D}$ and $n^o El\Gamma_{3D}$ are the number of faces of the 2D and 3D interfaces, respectively. The sampleLocation is the x-coordinate of the sampling sensor, $\Delta_y/2$ is the y-coordinate of the sampling sensor as Δ_y is the mesh discretization along w-axis, $z[i]$ is the z-coordinate of the cell i of the sampling sensor along z,

Algorithm 1: $\alpha_{\Gamma_{3D}}$ Boundary condition.

Step 1:
    sampleLocation = read(inputLocation);
Step 2:
if t = *first time step* **then**
    for $i \in n^o El\Gamma_{2D}$ **do**
        sampleVector = (sampleLocation, $\Delta_y/2$, $z[i]$);
        cell[i] = findNearestCell(sampleVector);
    end
end
Step 3:
for $i \in n^o El\Gamma_{2D}$ **do**
    $\alpha_{\Omega_{2D}}$[i] = α_{cell}[i]
    for $j \in \frac{n^o El\Gamma_{3D}}{n^o El\Gamma_{2D}}$ **do**
        $\alpha_{\Gamma_{3D}}$[i $\frac{n^o El\Gamma_{3D}}{n^o El\Gamma_{2D}}$ + j] =$\alpha_{\Omega_{2D}}$[i]
    end
end

2.5.2 Velocity at Γ_{3D}

Similar to the previous BC, the velocity boundary condition allows to transfer U from 2D to 3D and to absorb the reflective wave patterns in the 3D region at the same time. The active absorption is based on the shallow water theory (i.e., Higuera et al. (2013a)). The scheme of how the generic variable is transferred is shown in Figure 3. The expression for the velocity at the Γ_{3D} is as follows:

$$\mathbf{U} = \left(\mathbf{U}_{\Omega_{2D}} + \sqrt{\frac{g}{(h+\eta_{\Gamma_{3D}})}}(\eta_{\Gamma_{3D}} - \eta_{Gauge_{3D}}) \cdot \hat{\mathbf{n}}\right)\alpha_{\Omega_{2D}} \tag{6}$$

where $U_{\Omega_{2D}}$ is the velocity vector sampled at the sampling cells in Ω_{2D}, $h + \eta_{\Gamma_{3D}}$ is the total water level at the Γ_{3D}, $\eta_{\Gamma_{3D}}$ is the free surface elevation at the 3D interface, $\eta_{Gauge_{3D}}$ is the free surface elevation at the adjacent cells of the 3D interface (adjacent cells on the 3D side), h is the still water level, g is the z-component of the gravity acceleration and $\hat{\mathbf{n}}$ is a vector with components (1,0,0) such that the active absorption correction is applied to the x-component (streamwise) only. From Equation 6 it can be noted that the 3D patch can be subdivided into sub-patches to improve the active absorption performance. In that case, Equation 6 is directly applied a number of times equal to the number of sub-patches. This allows to force the model to absorb the three-dimensional wave pattern radiated from the structures that could appear inside the 3D domain. The measured free surface is thus calculated at each sub-patch and the velocity correction is different for each of them. Note that the number of sub-patches should be an integer multiple between 1 and up to the number of cells in the y-direction of the 3D interface (spanwise).

The way this BC works is summarised as follows:

- *step 1:* Reads the position of the sampling cells, i.e. x(m) Gauge 2D
- *step 2:* Searches for all nearest cell centres along z-axis for x(m) of Gauge 2D
- *step 3:* Collects vector with velocity values at the cell centres for each cell and transfers the information (collected vector) to the 3D interface (matching interfaces, no interpolations are needed) and sums the active absorption velocity. Note that the ratio $\frac{n^o El\Gamma_{3D}}{n^o El\Gamma_{2D}}$ represents the number of faces of the 3D patch in the y-direction (spanwise).

The Algorithm 2 shows the steps needed to transfer the velocity from the sampling cells in Ω_{2D} to Γ_{3D}.

Algorithm 2: $\mathbf{U}_{\Gamma_{3D}}$ Boundary condition.

Step 1:
    sampleLocation = read(inputLocation);
Step 2:
if t = *first time step* **then**
    for $i \in n^o El\Gamma_{2D}$ **do**
        sampleVector = (sampleLocation, $\Delta_y/2$, $z[i]$);
        cell[i] = findNearestCell(sampleVector);
    end
end
Step 3:
for $i \in n^o El\Gamma_{2D}$ **do**
    $\mathbf{U}_{\Omega_{2D}}$[i] = $\mathbf{U}_{cell}$[i] ;
    for $j \in \frac{n^o El\Gamma_{3D}}{n^o El\Gamma_{2D}}$ **do**
        $\mathbf{U}_{\Gamma_{3D}}[i \cdot \frac{n^o El\Gamma_{3D}}{n^o El\Gamma_{2D}} + j] = \left(\mathbf{U}_{\Omega_{2D}}[i] + \sqrt{\frac{g}{(h+\eta_{\Gamma_{3D}})}}(\eta_{\Gamma_{3D}} - \eta_{Gauge_{3D}}) \cdot \hat{\mathbf{n}}\right)\alpha_{\Omega_{2D}}[i]$
    end
end

2.5.3 *Pressure at Γ_{2D} and Γ_{3D}*

Regarding the pressure in excess of hydrostatic p^*, the gradient is set such that the velocity flux on the boundary is that specified by the velocity boundary condition. The BC reads as follows:

$$\frac{\partial p^*}{\partial n} = \left(\frac{\mathbf{H}}{a_p} \cdot \mathbf{S}_f - \mathbf{U} \cdot \mathbf{S}_f\right)\frac{a_p}{|\mathbf{S}_f|} \tag{7}$$

where $\mathbf{H}$ represents the terms off the diagonal of the matrix of the semi-discretised momentum equation, a_p are the diagonal terms of the same matrix, $\mathbf{S}_f$ is the area vector and $\mathbf{U}$ is the velocity field. The reader is referred to the source code of OpenFOAM (*https://www.openfoam.com/*) for the reference of the boundary condition.

2.5.4 Turbulent quantities

In Part I the laminar solution is used as no turbulent flows occur, while for many applications in Part II the turbulence has been modelled by using a stabilized $k - \omega$ model. In the following it is explained how turbulent quantities are dealt with at the interfaces for the one-way coupling used in Part II. In particular, zero gradient boundary conditions have been used for k and ω, while ν_T is directly calculated from k and ω. The same BCs are used for both the 2D and 3D interfaces. Note that the turbulence model can be enabled or disabled in each subdomain (i.e. 2D or 3D). It means that it can also be used for modelling the near field only. This allows to further reduce the computational time for those cases where a laminar flow in the far field suffice. It also represents an advantage of the coupled models as the over-production of turbulence can thus be avoided in the far field. The BCs read as follows:

$$\begin{aligned} \frac{\partial k}{\partial n} &= 0 \\ \frac{\partial \omega}{\partial n} &= 0 \\ \nu_T &= \frac{k}{\omega} \end{aligned} \tag{8}$$

2.5.5 Other boundary conditions at Γ_{2D}

The remained boundary conditions to be specified at Γ_{2D} are α and $\mathbf{U}$. The volume fraction is defined as zero gradient while the active absorption is used for the velocity boundary conditions. The active absorption at Γ_{2D} reads as follows:

$$\mathbf{U} = \sqrt{\frac{g}{(h+\eta_t)}}(\eta_t - \eta_c)\hat{\mathbf{n}} \tag{9}$$

where η_t is the target water level at the Γ_{2D}, η_c is the measured one at the adjacent interface cells, g is the z-component of the gravity acceleration and h is the still water level.

The flow direction and the number and types of boundary conditions used in this work are summarised in Table 2. The second and third columns in Table 2 refer to the 2D and 3D coupled interfaces, respectively.

2.6 The "two-way" coupling procedure

The two-way coupling scheme proposed in this work is explained in detail in Figure 4. Here, it can be observed that the generic variable (ϕ_n) can be transferred in two directions, i.e. from 2D to 3D and vice-versa. In the present work, the interfaces Γ_{2D} and Γ_{3D} have to match in the vertical direction z (adjacent cells), while different discretizations are allowed in streamwise (x)

Coupling directions	BCs Γ_{2D}	BCs Γ_{3D}
2D → 3D	$\frac{\partial \alpha}{\partial n} = 0$	$\alpha = \alpha(\Omega_{2D})$
	$\mathbf{U} = \sqrt{\frac{g}{(h+\eta_t)}}(\eta_t - \eta_c)\hat{\mathbf{n}}$	$\mathbf{U} = \left(\mathbf{U}_{\Omega_{2D}} + \sqrt{\frac{g}{(h+\eta_{\Gamma_{3D}})}}(\eta_{\Gamma_{3D}} - \eta_{Gauge_{3D}}) \cdot \hat{\mathbf{n}}\right)\alpha_{\Omega_{2D}}$
	$\frac{\partial p^*}{\partial n} = \left(\frac{\mathbf{H}}{a_p} \cdot \mathbf{S}_f - \mathbf{U} \cdot \mathbf{S}_f\right)\frac{a_p}{\lvert\mathbf{S}_f\rvert}$	$\frac{\partial p^*}{\partial n} = \left(\frac{\mathbf{H}}{a_p} \cdot \mathbf{S}_f - \mathbf{U} \cdot \mathbf{S}_f\right)\frac{a_p}{\lvert\mathbf{S}_f\rvert}$
if turbulence activated	$\frac{\partial k}{\partial n} = 0$	$\frac{\partial k}{\partial n} = 0$
	$\frac{\partial \omega}{\partial n} = 0$	$\frac{\partial \omega}{\partial n} = 0$
	$\nu_t = \frac{k}{\omega}$	$\nu_t = \frac{k}{\omega}$

Table 2: Coupling directions and boundary conditions at the interface boundaries Γ_{2D} and Γ_{3D}: **One-way** coupling. η_t and η_c refer to the target and calculated level at the 2D coupled interface (outlet of the 2D domain).

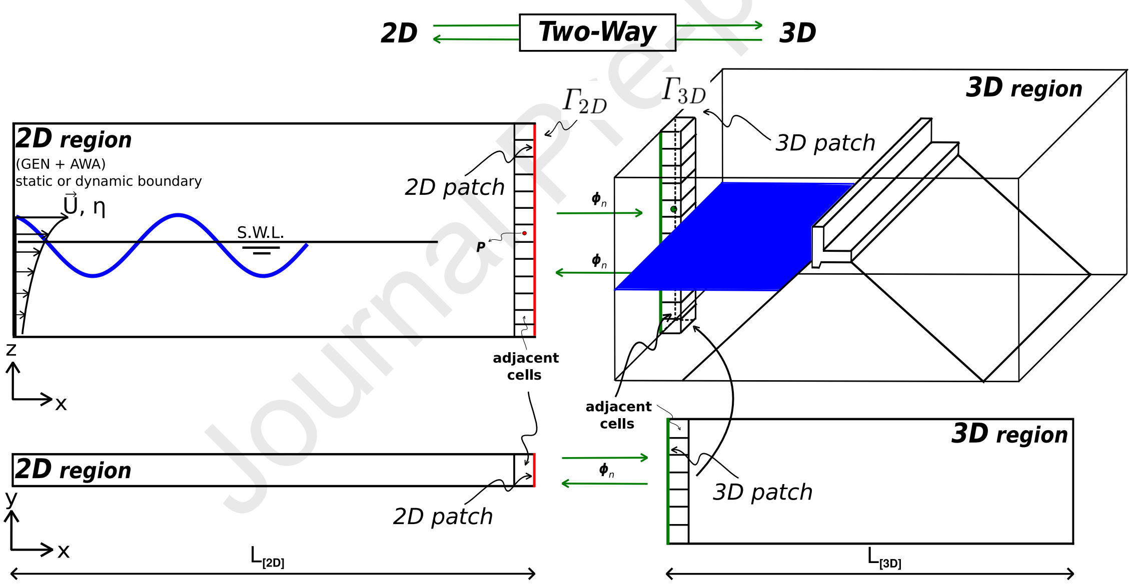

Figure 4: Two-way (bi-directional or strong) coupling scheme implemented in OpenFOAM® (v1812) framework.

and spanwise (y) directions. In addition, different number of cells in y are allowed to achieve the 2D-3D geometry.

A Robin-Robin coupling algorithm has been derived as in the work of Ferrer et al. (2016), that proposed a multi-region coupling methodology for incompressible/compressible solvers. However, this method has only been used in a 3D-3D approach, in which a single mesh based domain was built. No discussions on 2D-3D applications or partitioned segregated approaches were made. In the study of Ferrer et al. (2016), a single mesh was built and then divided into different regions (3D). By doing so, no different discretization in spanwise direction was allowed in the work of

Ferrer et al. (2016). Therefore, one of the main objectives of the present work is to extend the strong-coupling for applications in which the 2D and 3D meshes are built separately.

The idea of the coupling strategy was derived from the spatial derivative terms of the transport equations. By applying the Gauss's theorem the divergence becomes:

$$\int_V \nabla \cdot \phi dV = \int_S d\mathbf{S} \cdot \phi = \sum_{i=0}^{N} \mathbf{S}_f \cdot \phi_f \tag{10}$$

while the gradient operator reads:

$$\int_V \nabla \phi dV = \int_S d\mathbf{S} \phi = \sum_{i=0}^{N} \mathbf{S}_f \phi_f \tag{11}$$

and the Laplacian is:

$$\int_V \nabla \cdot (\nabla \phi) dV = \int_S d\mathbf{S} \cdot (\nabla \phi) = \sum_{i=0}^{N} \mathbf{S}_f \cdot (\nabla \phi_f) \tag{12}$$

where V is the control volume, ϕ the generic variable calculated at the cell centre, $\mathbf{S}_f$ the face area vector and ϕ_f the generic variable calculated at the face centre and N is the number of faces.

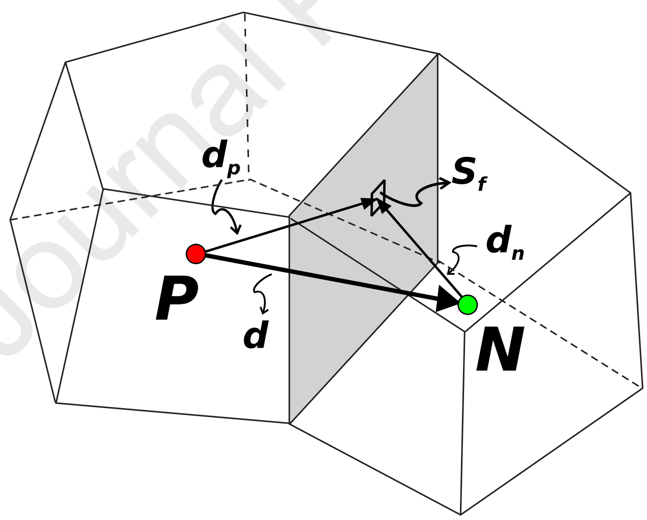

Figure 5: Finite volume discretization. Two generic adjacent cells (P and N) to the coupled interfaces are shown.

2.6.1 *Generic variable boundary condition* $\phi(\Gamma_{iD})$

At this step, the scheme for ϕ_f and $\nabla \phi_f$ is to be defined. According to Ferrer et al. (2016) the value of the magnitude of ϕ at the interface is a distance-weighted average between two adjacent cells (see Fig. 5), as follows:

$$\phi_f = \frac{1}{|\mathbf{d}_p| + |\mathbf{d}_n|} (\phi_p |\mathbf{d}_n| + \phi_n |\mathbf{d}_p|) \tag{13}$$

and the gradient at the interface as:

$$\mathbf{S}_f \nabla \phi_f = (|\mathbf{S}_f| \frac{\phi_p - \phi_n}{|\mathbf{d}|})(-\frac{\mathbf{S}_f \cdot \mathbf{d}}{|\mathbf{S}_f||\mathbf{d}|}) \tag{14}$$

for the region containing the cell N, and,

$$\mathbf{S}_f \nabla \phi_f = (|\mathbf{S}_f| \frac{\phi_n - \phi_p}{|\mathbf{d}|})(\frac{\mathbf{S}_f \cdot \mathbf{d}}{|\mathbf{S}_f||\mathbf{d}|}) \tag{15}$$

for the region containing the cell P. As indicated in Figure 5 d is the vector between two adjacent cell centres, d_n and d_p are the face-cell distances and S_f is the face area vector. All BCs used for each field are summarised in Table 3. The BC works both for scalar fields (α, p^*, k and ω) and vectors (**U**).

When applying the above BC to the 2D patch, the neighbour cells considered are the adjacent cells (central column of cells).

The above implementations are extensively validated for the 3D-3D approach in Ferrer et al. (2016). An additional goal of this work is to validate the coupling for a 2D-3D approach. In Table 3 the variable ϕ represents the generic variable for which the BC is applied (e.g.α, **U**, p_d, k, ω).

Coupling directions	**BCs** Γ_{2D}	**BCs** Γ_{3D}
2D $\rightleftarrows$ 3D	$\phi = \frac{1}{\lvert\mathbf{d}_p\rvert+\lvert\mathbf{d}_n\rvert}(\phi_p\lvert\mathbf{d}_n\rvert + \phi_n\lvert\mathbf{d}_p\rvert)$	$\phi = \frac{1}{\lvert\mathbf{d}_p\rvert+\lvert\mathbf{d}_n\rvert}(\phi_p\lvert\mathbf{d}_n\rvert + \phi_n\lvert\mathbf{d}_p\rvert)$
	$S_f \nabla\phi = \lvert\mathbf{S}_f\rvert \frac{\phi_n - \phi_p}{\lvert\mathbf{d}\rvert} \frac{\mathbf{S}_f \mathbf{d}}{\lvert\mathbf{S}_f\rvert\lvert\mathbf{d}\rvert}$	$\mathbf{S}_f \nabla\phi = \lvert\mathbf{S}_f\rvert \frac{\phi_p - \phi_n}{\lvert\mathbf{d}\rvert}(-\frac{\mathbf{S}_f \mathbf{d}}{\lvert\mathbf{S}_f\rvert\lvert\mathbf{d}\rvert})$

Table 3: Coupling directions and boundary conditions at the interface boundaries Γ_{2D} and Γ_{3D}: **Two-way** coupling. The generic variable (scalar or vector) is indicated with ϕ.

The generic boundary condition for the two-way coupling can be applied to scalars, vectors or tensor quantities.

2.7 *The coupled solver*

To solve the coupled simulations a coupled solver is implemented as shown in Figure 6. The solver allows to resolve different sets of equations in each sub-domain, although in this study only a RANS-RANS approach is used. First, the meshes are created and next the fields are initialised (Figure 6, left box). The initial time step is calculated based on the minimum resulting Courant number (Co) between the 2D and the 3D regions. VOF equation is solved using the MULES algorithm. PIMPLE algorithm (i.e., a combination of PISO and SIMPLE algorithms, Issa (1986) and Patankar and Spalding (1983), respectively) is used to solve pressure-velocity. PIMPLE can be used in PISO mode as shown in the flow-chart of Figure 6 or in PIMPLE mode applying multiple pressure-velocity correction iterations. The above procedure is repeated for each 2D and 3D regions until the current time is equal to the end time of the simulation. PIMPLE in PISO mode has been used in Part I.

2.8 *Application of one-way and two-way boundary conditions*

In OpenFOAM the BCs are applied by calling the function *correctBoundaryConditions()*. For example, when applying velocity boundary conditions we call *U.correctBoundaryConditions()*. The coupling boundary conditions are generally updated when the equations are solved. Particularly, level boundary conditions (volume fraction based BCs) are applied when VOF equation is solved. Velocity and pressure BCs are updated (calculated) when momentum and pressure correction (Laplace equation) are solved. Finally, turbulence quantities are calculated when the turbulence equations are used. In the present work each boundary condition has been applied at least three times per time step both when PISO or PIMPLE modes were used.

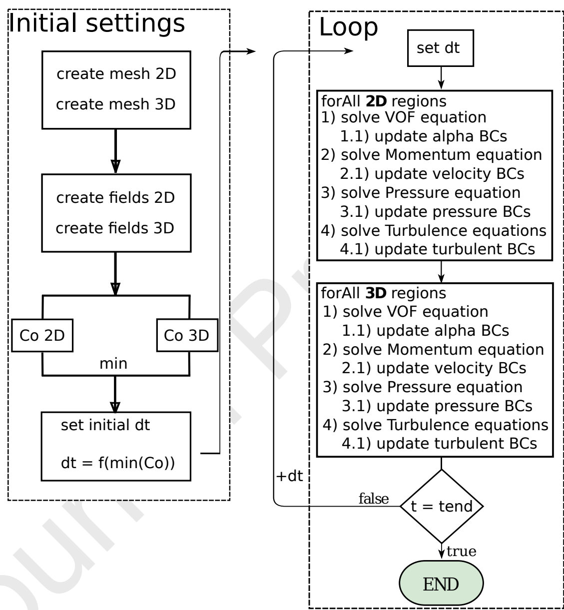

Figure 6: Flow chart of the multi-region solver implemented in OpenFOAM®.

3 Validation and analysis of the coupling methodologies

Several validation cases have been developed, such as, waves propagating on an horizontal bottom in an empty numerical domain. These benchmark cases are key to verify the capability of the coupling schemes to reproduce wave patterns with very high accuracy and without introducing disturbances at the coupling boundaries. Because the proposed models are intended to be used when a high accuracy in simulating the hydrodynamics is needed, non-linear waves as well as a second order wave generation method for bichromatic and focused wave groups (considering both sub-harmonics and super-harmonics interactions) have been considered. These kind of waves are challenging to generate with simplified models which approximate the hydrodynamics. For example, it is crucial to verify the ability of the coupled models to ensure the transfer of the focused wave group including gravity and infragravity wave energy and the interaction between them. This aspect will be briefly discussed later in the paper. The validation cases have been defined for varying wave heights, periods and water depth, as summarised in Table 4. Static boundaries have been used for generated non linear waves. Regarding the second order generation method (focused and bichromatic waves), the moving boundary technique (Higuera et al. (2015)) has been applied to simulate the wave-maker motion. The second order transfer function proposed by Schäffer and Steenberg (2003) has been used to characterise the second order wave-maker motion. The comparisons against experimental results for the validation cases are out of the scope as the CFD models used in this work have been extensively validated in the past both for wave generation and wave structure interaction (e.g. Higuera et al. (2013a), Higuera et al. (2013b), Higuera et al. (2014a), Higuera et al. (2014b), Higuera et al. (2015)). Numerical results will be used to provide comparisons between 3D (without any coupling), one-way and two-way simulations as the main objective of the following part is to validate the quality of the couplings for transferring flow information.

The numerical domains for the one-way and two-way methodologies are shown in Figure 7. A 20m long, 0.04m wide (1 cell) and 1m high numerical domain (x-z plane) has been defined for the 2D region, while a 20m long, 0.4m wide (10 cells), 1m high domain has been built for the 3D region. The number of cells in y-direction (spanwise) has been limited to 10 to speed-up computation and it is further justified by the fact that no 3D effects are expected. Previous studies indicate that a number between 8 and 12 cells per wave height is needed for accurately generate the target wave patterns (e.g. Simonetti et al. (2018), Jacobsen et al. (2012), Larsen and Fuhrman (2018)). In this work, a number of 10 cells per wave height has been defined for wave propagation to not excessively increase the computational time and to respect the range mentioned above. Aspect ratios (Δ_x/Δ_z) of 1, 2 and 4 have been considered preliminarily. As the results do not significantly change for the ratios considered we applied the highest one, i.e. Δ_x/Δ_z=4, to further speed-up the simulations. The Δ_y is 0.04m and the total span-wise is 0.4m (10 cells). The C_o numbers used are reported in Table 6.

Wave generation and active wave absorption (using shallow-water theory) have been defined at the inlet boundary (on the left). Active wave absorption has been used at the outlet of the 2D region (only in the case of one-way mode).. The one-way boundary conditions implemented are applied at the 3D side of the coupled interfaces and allow to transfer waves from 2D to 3D and absorb the reflected pattern inside the 3D. On the other hand, the two-way BCs are identically applied at both 2D and 3D interfaces and allow waves to travel from 2D to 3D and vice-versa. The outlet patch of the 3D domain is defined as an active absorption boundary under the assumption of shallow water conditions. The lower boundary (bottom) has been set as impermeable and the top has been defined as atmosphere.

Figures 7 shows the numerical domains built to perform the simulations. For the one-way scheme the interfaces are located at the middle of the numerical domain ($x_1 = 20m$), and the position of the sampling sensor (WG1) is at $x_2 = 19.02m$. In order to build an equivalent two-way scheme, the coupled interfaces must be located at the position of the sampling sensor used for the one-way approach (i.e. $x_2 = 19.02m$). By doing so, the spatial domains for the one-way and two-way are different as shown in Figure 7 (panels a and b, respectively). As the coupled interfaces are shifted in the two approaches (i.e. $x_1 = 20m$ for one-way and $x_2 = 19.02m$ for two-way), the wave gauges will also be shifted of the quantity $x_1 - x_2$. The positions of wave gauges are shown in Figure 7, panels a and b for the one-way and two-way approaches, respectively. The numerical domain used for the full 3D simulations is long as the two-way one (panel b), but obviously it is built in a single-domain.

Firstly, comparison of free surface are shown at the coupling zone WG2. Secondly, free surface elevation, velocity and dynamic pressure profiles are displayed comparing the measurements at the WG1 (2D region) and WG3 (far field in 3D region).

The simulations have been performed in three different modes:

- 2D-3D one-way (two domains)
- 2D-3D two-way (two domains)
- 3D (one domain)

The main objective is to obtain for the 2D-3D coupled models and the same results as for the full 3D simulations.

For the full 3D case all the numerical parameters described above have been used (meshes, Co number, etc.). Table 4 includes the numerical tests carried out.

N	**Case**	h**[m]**	H**[m]**	T**[s]**	H/L**[-]**	H/h**[-]**	H_1**[m]**	H_2**[m]**	T_1**[s]**	T_2**[s]**	f_c**[Hz]**	Δ_f**[Hz]**	N**[-]**
1	Solitary	0.6	0.1	-		0.17							
2	Stokes II	0.6	0.05	2.5	0.009	0.08							
3	Stokes II	0.6	0.10	2.5	0.018	0.17							
4	Stream F.	0.4	0.152	3.02	0.026	0.375							
5	Solitary	0.6	0.35	-		0.58							
6	Cnoidal	0.4	0.12	2.2	0.03	0.3							
7	Cnoidal	0.4	0.15	4	0.015	0.375							
8	Bichromatic	0.4	-	-	-	-	0.05	0.05	1.8	2.1			
9	Focusing	0.4	0.1	-	-	-	-	-	-	-	0.505	10	50
10	Solitary	0.5	0.15										
11	Stream F.	0.5	0.15	3	0.023	0.3							

Table 4: Wave conditions simulated in one-way, two-way and 3D modes.

3.1 Free surface, velocity and dynamic pressure

In the following, comparisons are provided at two positions, i.e. at the coupling zone WG2 and 10.5m far from the coupling interfaces WG3. The position $x = 30.5m$ has been chosen to be far enough from the coupling boundary and outlet patch of the 3D domain, to reduce disturbances induced by the boundary conditions and not to be influenced by the coupling BCs. Figure 8 shows comparisons of the free surface elevation at the coupling interfaces WG2 in Fig. 7) obtained from the one-way, two-way and the full 3D simulations, for the first six validation cases listed in Table 4 (non-linear waves).

Figure 8 shows a good correspondence between the 3D simulations and the coupled models (weak and strong). In particular, wave crests and troughs are close to the three dimensional solution, and the wave asymmetries and non linearities are well reproduced. By investigating the

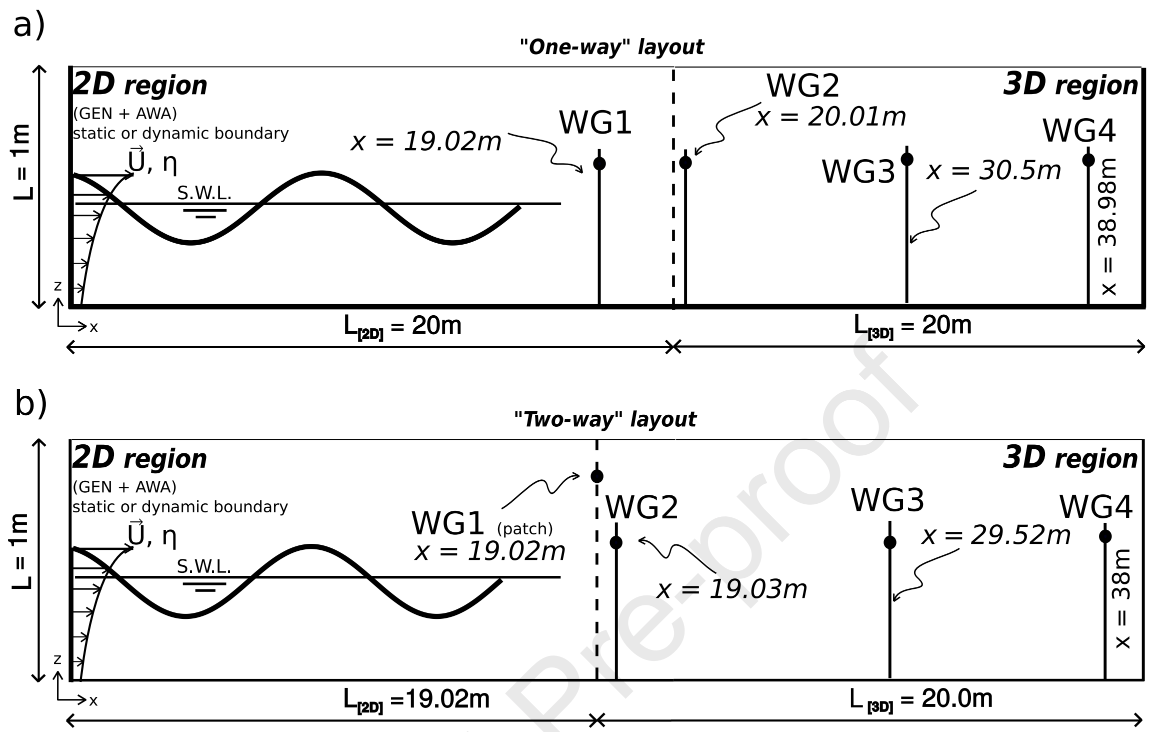

Figure 7: Panel a: Numerical domain used for the one-way simulations. The dashed black-line indicate the position of the 2D-3D coupled interfaces. The position of sampling sensor WG1 (sampling patch in Figure 2) is also indicated. Panel b: Numerical domain used for the two-way simulations. The dashed black-line indicate the position of the 2D-3D coupled interfaces. The position of sampling sensor WG1 (sampling patch in Figure 4) is also indicated.

propagation of a solitary wave (panel a), it can be noted that the discrepancies between the proposed models and the 3D solution are small. A good match of the wave crest is shown, as well as the wave disturbances that follow the wave crest. In addition a very small phase lag is observed for the numerical results of the one-way simulation. The second validation case is based on a non-linear second order Stokes-wave with wave height $H = 0.05m$, wave period $T = 2.5s$, water depth $h = 0.6m$, wave steepness $H/L = 0.009$ and wave non-linearity $H/h = 0.08$. Panel b of Figure 8 shows a good prediction of free surface elevation for all simulations (one-way and two-way) compared to the 3D case. On average, wave crests and troughs are well predicted by both the one-way and two-way models, and is very small. However, the one-way model appears to slighlty over-predict crests and troguhs due to the active wave absorption, although the difference is small compared to the 3D results. The third validation case is based on the non-linear second order Stokes-wave, with wave height $H = 0.1m$, wave period $T = 2.5s$ and water depth $h = 0.6m$. Here, the wave steepness is doubled ($H/L = 0.018$) and non-linearity is increased ($H/h = 0.08$). Panel c of Figure 8 shows the results of the simulations with a good prediction of the free surface elevation in all cases (one-way and two-way). The two-way coupled model matches the 3D data well throughout the simulation. A good correlation is also obtained with the one-way model although very small under-prediction of the last three troughs can be observed ($33s < t < 40s$). It

556 may be due to the wave reflection from the outlet of the 2D region. However, the discrepancy appears to be small and as it will be demonstrated later in this paper and its companion (Part II) the active absorption does not affect results significantly, also considering different hydrodynamics and long time series of waves.

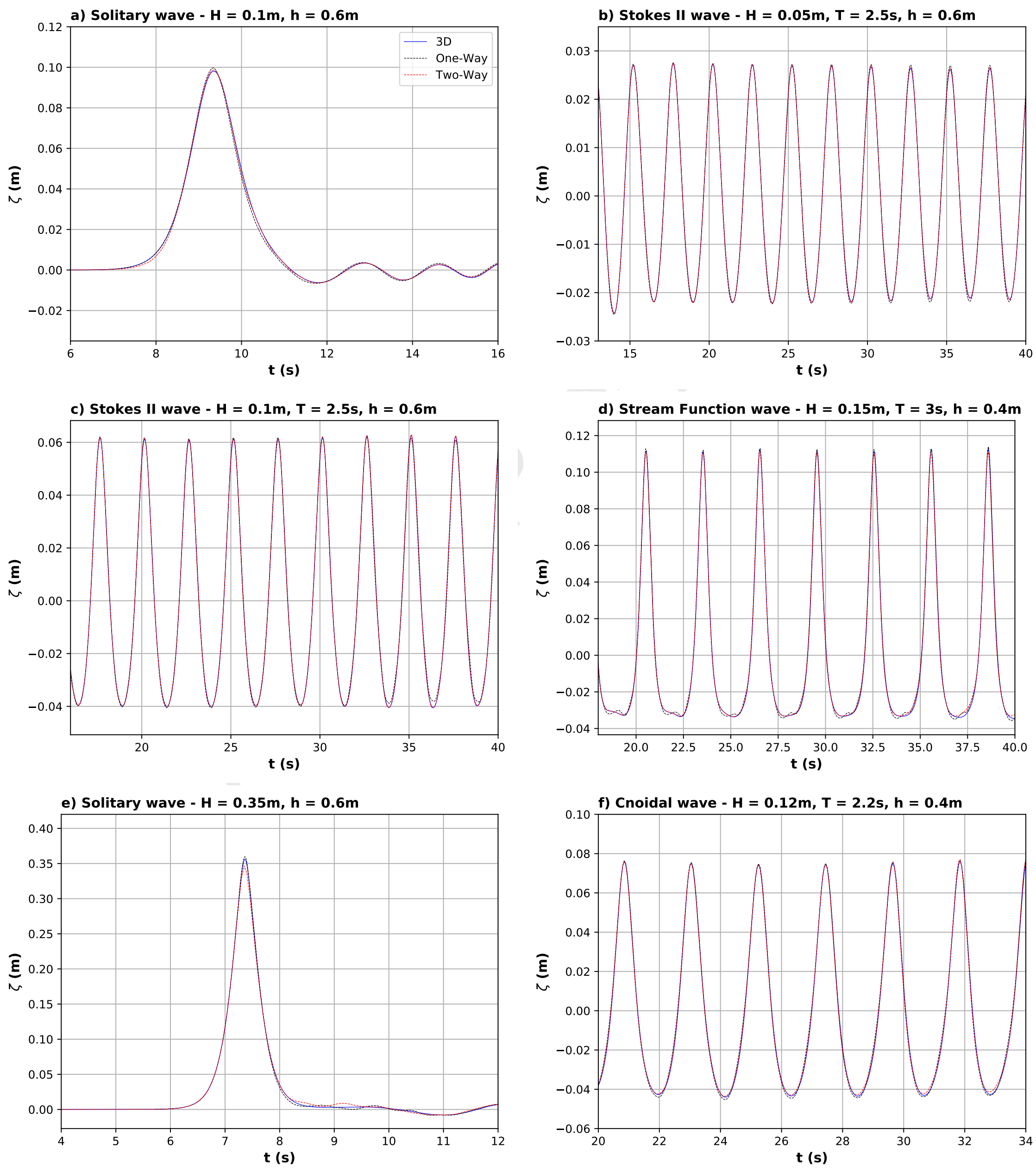

Figure 8: Free surface comparison between One-way (dashed black-line), Two-way (dashed red-line) and full 3D (continuous blue line) simulations at gauge WG2, located close to the 3D interface (see Figure 7).

The fourth validation case is based on the non-linear Stream Function Theory, with wave height $H = 0.15m$, wave period $T = 3s$ and water depth of $h = 0.4m$. The resulting wave steepness ($H/L = 0.026$) and wave non-linearity ($H/h = 0.375$) are increased. Firstly, by observing panel d) of Figure 8, it is evident that the coupled models accurately simulate the wave heights and again, the phase shift is very small. By comparing the results of coupled models (both one-way and two-way) with the 3D data, it can be seen that the wave crests and the troughs are well-predicted throughout the simulation. Small discrepancies are obtained comparing the shape of the troughs. The one-way simulation shows small different in the shape of the troughs throughout the simulation, while on average the two-way solution is more in line with the 3D data. Also, the two-way model shows very small under-prediction of the wave crests, while the one-way model displays a better match in this case.

The fifth validation case is based on Boussinesq theory for a solitary wave, but in this case very shallow water conditions have been simulated. A high ratio $H/h = 0.58$ is considered to test the stability of the code. Figure 8, panel e) presents good correlation between one-way, two-way and 3D results for free surface elevation. The two-way models seems to under-predict the wave peak while the one-way simulation slightly over-predict it. However, note that the discrepancy is acceptable as the error is always below 10%.

The sixth validation case considered is based on the Cnoidal-wave theory with wave height $H = 0.12m$, wave period $T = 2.2s$ and water depth of $h = 0.4m$ resulting in a high ratio of wave steepness ($H/L = 0.03$). From the inspection of panel f) of Figure 8 a good comparison between the coupled models and the 3D solution is obtained. Very small discrepancies appear for the amplitudes of the wave troughs predicted using the coupled models. The wave height is not damped throughout the simulations and the wave crests are correctly reproduced with all models.

Two additional validation cases have been performed considering second order wave generation (Table 4). A focused wave group and a bichromatic wave group are generated as it is key to verify the ability of the coupled models to ensure the energy transfer between gravity and infra-gravity waves.

Figure 9 shows comparisons of the free surface elevation at the coupling zone as well as far from the coupled interfaces. The first case studied is wave focusing. A large transient wave group characterised by 50 components ($N_{comp} = 50$), a central frequency $f_c = 0.505Hz$ and a frequency bandwidth $\Delta f_c = 0.10Hz$ is generated. The wave height of the group is $H = 0.10m$ (50 amplitude components (N_{comp}) $a_n = 0.1/50 = 0.002m$) and the water depth is $h = 0.4m$. The focus position is $x_f = 30.5m$ and the time at which the wave focusing occurs is $t_f = 50s$. Thus, the wave focusing occurs inside the 3D domain ($x_f = 30.5m$). Figure 9 shows results of the free surface elevation resulting from the focused wave at WG2 and WG3. In each panel it is shown, the total free surface elevation (free surface) and the bound long wave amplified by a factor of 10 (bound long wave (x10)). According to previous research (i.e. Lara et al. (2011b)) the infragravity bound long wave, which is induced by the radiation stress gradient of the short wave group, is determined by low-pass filtering with a cut-off frequency of $f_c/2$. Panel a) shows a good correspondence between the 3D solution and the coupled model, both for the measured free surface elevation and the bound long wave. The discrepancy between the one-way, two-way and 3D results is small. To complete

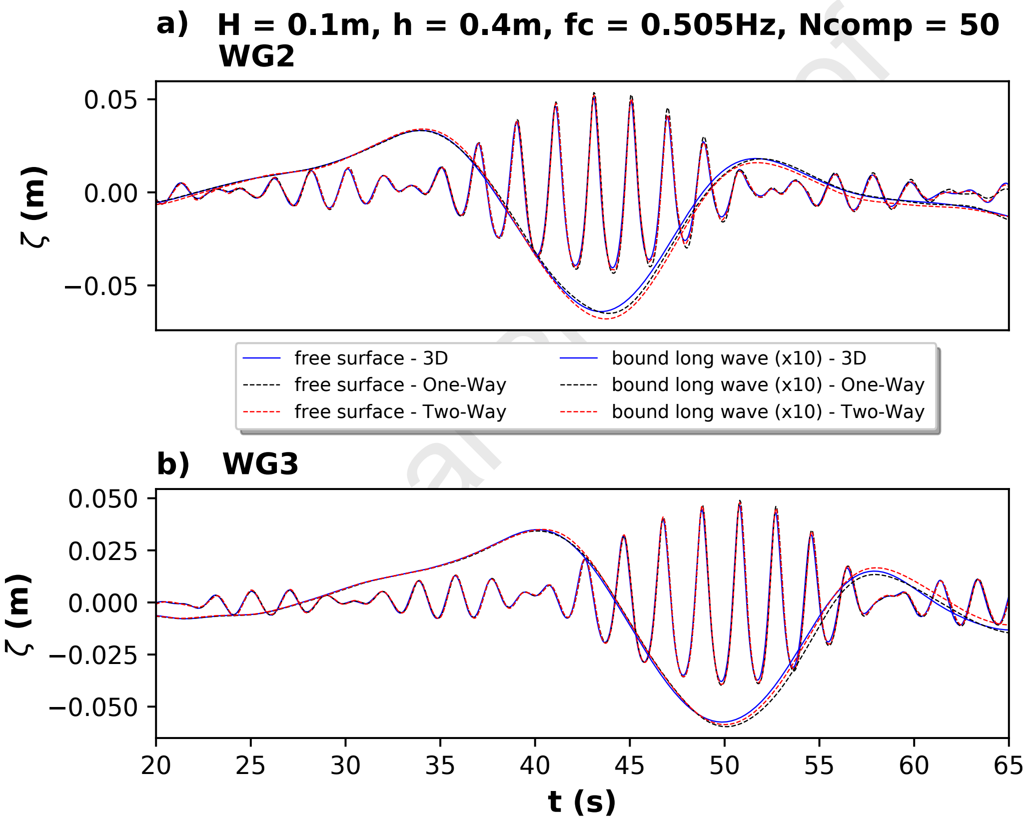

Figure 9: Free surface elevation for one-way, two-way and 3D simulations (dashed black, red and solid blue lines, respectively). The bound long wave is amplified by a factor of 10. Panel a and b show results at WG2 and WG3, respectively.

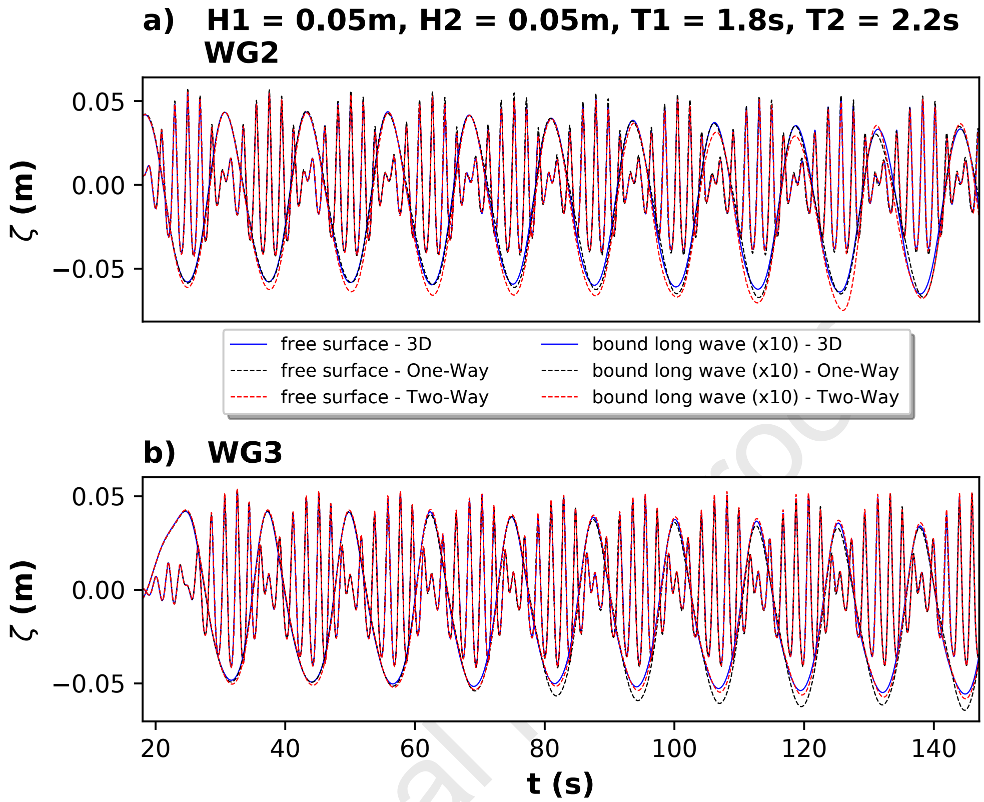

Figure 10: Free surface elevation for one-way, two-way and 3D simulations (dashed black, red and solid blue lines, respectively). The bound long wave is amplified by a factor of 10. Panel a and b show results at WG2 and WG3, respectively.

the validation of the focused event, the comparison of free surface at the focusing position ($x_f = 30.5m$) is shown in panel b). As for the results of panels a) , an good match is shown for the three simulations. In addition, it can be observed that the bound long wave trough becomes noticeable under the peak of the short wave group, according to the uniform depth solution of Longuet-Higgins and Stewart (1962) and the numerical model developed by Lara et al. (2011a). However, note that the scope of this part of the work was to check the capability of the coupled models to obtain results close to the 3D simulation, rather that analysing the hydrodynamics of infragravity waves, as the CFD model used has already been validated for focused wave groups (i.e. Higuera et al. (2015)). Therefore, an extensive hydrodynamic analysis of second order wave generation is out of the scope of this research.

The last case is the generation of a bichromatic wave group with $H_1 = 0.05m$, $H_2 = 0.05m$, $T_1 = 1.8s$, $T_2 = 2.1s$ in a water depth $h = 0.4m$. Results are shown in Figure 10. Ten groups are displayed in each panel (a and b). A good agreement is shown for the coupled models and the 3D results at the coupling zone (panel a), both for the total free surface and the bound long wave. For the bound long wave a good match is also observed although is observed that some discrepancies are clearly visible, particularly in the troughs obtained with the two-way model. It has to be kept in mind that the discrepancies are strongly amplified by a factor of 10. Results at 30.5m (panel b) show a small deviation of the one-way solution, which may be due to the absorption at the interface when the duration of time series becomes longer. The amplitudes of the troughs slightly increase with the simulation time. Here, the error for the bound long wave using the one-way model slightly exceed 10%. However, good results are generally obtained when second order wave generation is studied, considering both sub-harmonics and super-harmonics interactions also for long time series. In conclusion, the coupled models are able to pass information through the interfaces when highly non-linear waves including second order wave generation are considered. The two-way model appears to better perform when second order generation is used.

So far the validations have been made at the coupling zone for the first six cases in Table 4 and in the middle of the 3D domain for the second order generation cases (focusing and bichromatic). To conclude the validations, pressure and velocity profiles at a gauge placed far from the coupling interfaces ($x = 30.5m$) will also be shown. The comparison at a location far from the forcing BCs is more representative to check the stability of the waves generated (e.g. no damping). For the sake of brevity only four cases are shown in the following, considering low and high wave steepness and non-linearity.

Figure 11 shows a comparison of the free surface (ζ in m), dynamic pressure (p_d, obtained removing the hydrostatic part from the pressure in excess) (in m of water column) and horizontal velocity (U_x in m/s) for the solitary wave simulated in the one-way and two-way modes at x=30.5m. The wave non-linearity is $H/h = 0.17$. Free-surface elevation (panel a) shows a good match for the coupled models and the 3D simulation. The one-way results show a small delay of the wave crest and also small deviations of the shape. At $t = 13.35s$, which corresponds to the passage of the crest, the pressure and velocity profiles are compared. The dynamic pressure p_d shows good results for the three-dimensional simulation and the coupled models (panel b). Small deviations can be observed in the velocity profile (panel c) using the one-way model, although a very good correspondence is shown at the free surface and at the bottom. The deviations can be observed between the free surface and the bottom and may be due to numerical errors (e.g. numerical diffusion, discretization error). The deviations among models might also be due to the very small delays between signals (panel a).

Figure 12 shows the comparison of free surface, horizontal velocity and dynamic pressure results at $x = 30.5m$ for the Stokes II case with wave height $H = 0.05m$, wave period $T = 2.5s$ and water depth $h = 0.6m$ ($H/h = 0.08$, $H/L = 0.009$). Results of free surface elevation (panel a) are very satisfactory, as both wave crests and troughs are well captured, and the signals are aligned in time. Two instants of time are taken for comparing pressure and velocity. The passage of a crest ($t = 22.35s$) and a trough ($t = 23.6s$) are analysed in the following. Horizontal velocity profiles under a wave crest at $t = 22.35s$ (panel c) match well in magnitude. The peaks of the positive velocity are almost coincident, while some fluctuation appears below the free surface level. By observing the dynamic pressure at the same instant (panel b) it can be seen that a good correlation between the coupled and 3D models is shown, although the coupled solvers seem to slightly under-predict the pressure from below the crest to the bottom. Panel d shows a good agreement of the dynamic pressure for all simulations. Here, the two-way model slightly over-estimates the

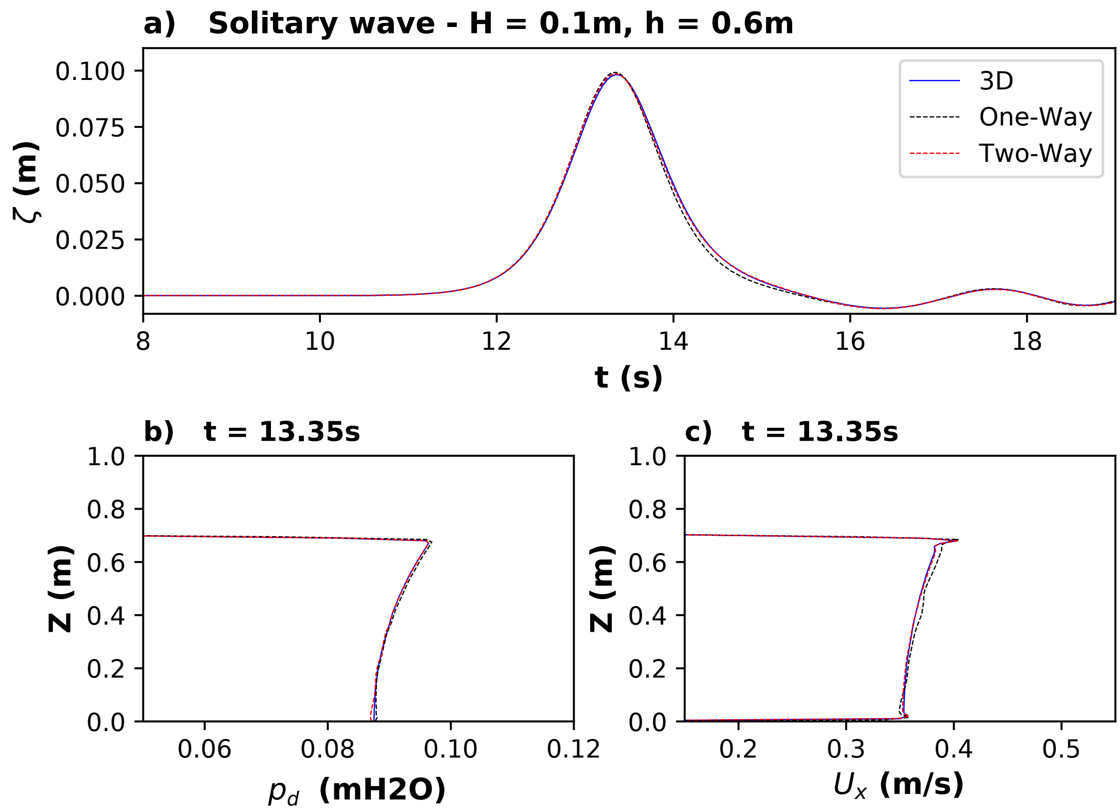

Figure 11: Solitary wave: H = 0.1m, h = 0.6m. Panels a), b) and c) comparison of free surface elevation, dynamic pressure and horizontal velocity profiles, respectively at WG3.

pressure. In addition, small oscillations are shown close to the bottom for both coupled models. The velocity profile (panel e) illustrates that close results are obtained for both coupled models, but some small discrepancies are shown (small underestimation) compared to the 3D data.

It is extremely important to point out that all numerical models (coupled and 3D) seem to slightly over-estimate the velocity near the free surface what has also been found by other authors, i.e. Larsen et al. (2019) (see Figure 4 of Larsen et al. (2019)). According to them the above problem was believed to arise from an imbalance in the discretised momentum equation near the interface and the occurrence high velocity at the mixture cells (air-water cells, i.e. $0 < \alpha < 1$). Larsen et al. (2019)reduced the overestimation of velocity at the water-air interface by lowering the Courant number up to 0.02. However, in the present work this effect is considered to be secondary, as the main objective is to demonstrate that the coupled models' results match well with the 3D solutions, although very small discrepancies persist. Certainly, this aspect has to be bear in mind to improve the quality of the CFD simulations.

Figure 13 shows the results from the case study 3 in Table 4. The simulation was based on the Stokes II theory, with wave height $H = 0.1m$, wave period $T = 2.5s$ and water depth $h =$

$0.6m$. Here the wave non-linearity and steepness are increased, $H/h = 0.08$ and $H/L = 0.009$, respectively. Good results of free surface elevation (panel a) are obtained. Wave crests and troughs are well captured and the signals without phase shift. As time goes the troughs predicted by the one-way model slightly differ from the ones obtained with the two-way coupling and the full 3D. It may be related to the active absorption correction which introduced a correction in the velocity profile. However, the effect seems to be small in this case. Panels b) and c) in Figure 13 illustrate the comparison of dynamic pressure and horizontal velocity, sampled below a wave crest. Fields under a wave trough are displayed in panels d and e. A good match for the dynamic pressure is shown between the coupled model and the 3D simulation throughout the simulation Horizontal velocity profiles at $t = 27.25s$ (panel c) match well in magnitude and a good correlation is also shown for the maximum velocity . A good match is observed at the upper part of the vertical profile whereas some small deviations are observed close to the bottom. Panel d) shows also good correlations for pressure comparison under the wave trough ($t = 28.4s$), although very small deviation are noted in the lower part of the profile, especially for the one-way results. Finally, panel e) displays the velocity profile under a wave trough. Again, a good correlation between the coupled and 3D results is displayed, although small deviations are observed for the two-way results in this case. The one-way model shows a small deviation from the 3D solution at the bottom, which might be caused by numerical errors (e.g. numerical diffusion, discretization error) as the upper part of the profile match the full solution very well.

Figure 14 displays results for a Cnoidal wave (in Table 4), with wave height $H = 0.12m$, wave period $T = 2.2s$ and water depth $h = 0.4m$. This case has been defined to obtain high wave steepness ($H/L = 0.03$) and non-linearity ($H/h = 0.3$) ratios. As for the previous cases, good results (panel a) are obtained for free surface elevation. A very small deviation is noted for the one-way results, particularly for the troughs. In addition the one-way model shows a very small delay in time. Panels b) and c) in Figure 14 depict the comparison of dynamic pressure and horizontal velocity. A good match for the dynamic pressure is shown between the one-way model and the 3D simulation, while the two-way simulation slightly under-estimates the pressure in this case. The velocity peak at $t = 30.65s$ (panel c) match well while discrepancies are observed between the bottom and z=0.4m. Good results are also observed for the wave trough analysed ($t = 27.2s$). Good correlation for the dynamic pressure (panel d) and velocity profile (panel e) are shown both for the 3D simulation and the coupled model results. Here, the pressure profiles obtained with the coupled model match the full solution very well, while some discrepancies are observed for the velocity profile between z=0m and z=0.4m.

The last case is the solitary wave simulation for which a very high wave non-linearity ($H/h = 0.58$) was considered. Figure 15 shows the main results. The simulation was based on the Boussinesq theory, with wave height $H = 0.35m$, and water depth $h = 0.6m$. Again, in line with previous results, a good correlation is found for free surface elevation (panel a) from the one-way, two-way and 3D results. The one-way model slightly under-predict the wave crest. A good match for the dynamic pressure is shown between the one-way model and the 3D simulation, while the two-way simulation slightly under-estimates the lower-part of the profile (close to the bottom) and over-estimates the maximum pressure under the crest. The horizontal velocity profiles at $t = 10.85s$

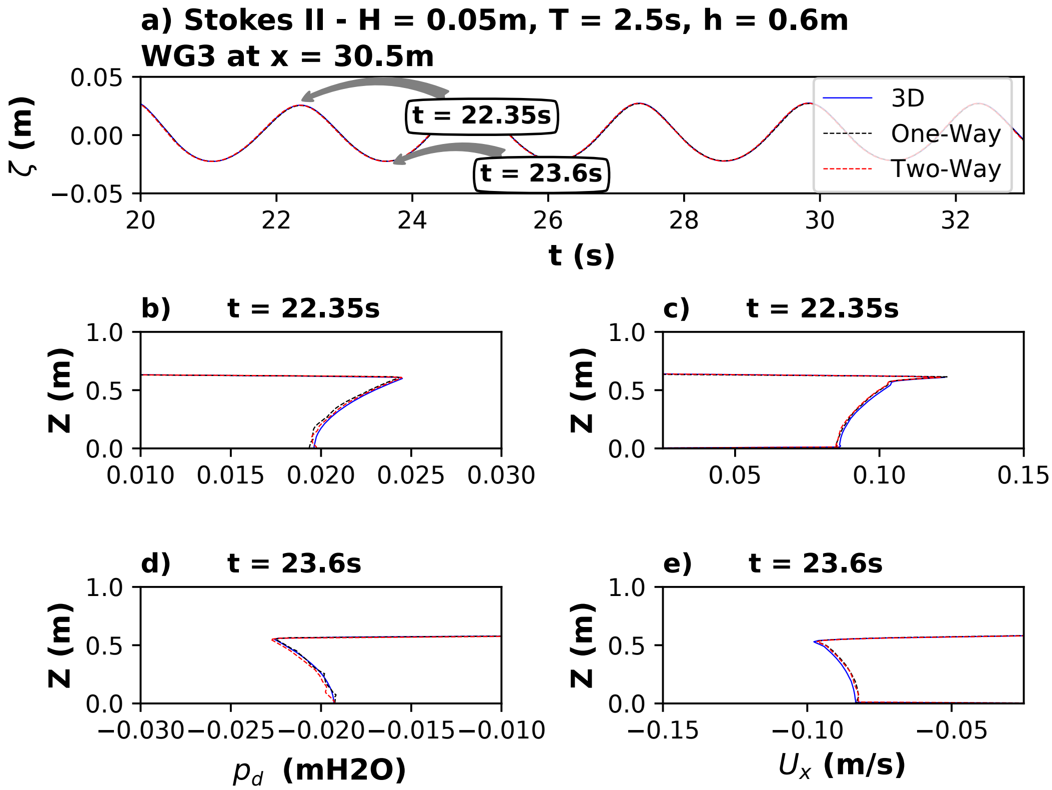

Figure 12: Stokes II regular waves: H = 0.05m, h = 0.6m, T = 2.5s. Panel a) comparison of free surface elevation, b) and d) dynamic pressure (in m of water column) and panels c) and e) horizontal velocity profiles at WG3.

(panel c), match well in magnitude while the peak estimation is acceptable when applying one-way or two-way couplings. The discrepancies observed are also accentuated by a small phase lag in the passage of the crest, especially for the one-way model (panel a). However, the error is below 6% for the worst scenario ($U_{x_{one-way}} = 1.47m/s$ and $U_{x_{3D}} = 1.56m/s$).

3.2 *Stabilisation of the two-way coupled model*

Here, it is important to specify that although good results are obtained with both coupled models, the two-way scheme appeared to be more unstable under extreme hydrodynamics. Such as, results for the Stream Function have been obtained with a low Courant number ($Co = 0.1$). By increasing the Co it has been be observed that the two-way coupled model became unstable. Spurious velocities at the air-phase can cause the model to become unstable (Figure 16).

Figure 16 shows that peaks of positive and negative velocities occur after the passage of the steep wave crest in particular on the 3D side for the same simulation but with $Co = 0.3$. In order to stabilise the model different solutions are proposed and listed as follows:

1. Apply a strong coupling using multiple iterations between momentum and pressure equations (PIMPLE) with under relaxation of velocity

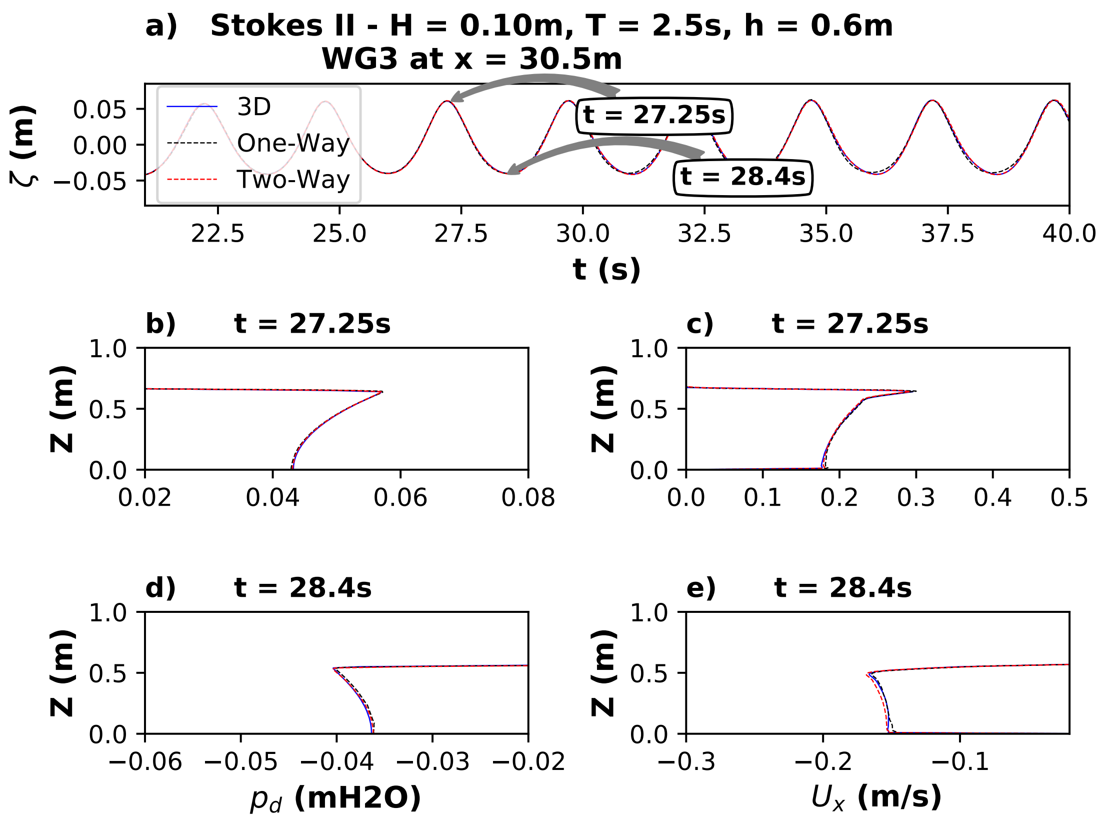

Figure 13: Simulation of Stokes II regular waves: H = 0.1m, h = 0.6m, T = 2.5s. Panel a) comparison of free surface elevation, b) and d) dynamic pressure (in m of water column) and panels c) and e) horizontal velocity profiles at WG3.

2. Apply a low Courant number and reduce the aspect ratio
3. Apply a stabilisation based on filtering air velocity at the two-way coupled interfaces

The first option has been successfully tested for the Stream-function wave simulated and it allowed to obtain a more stable model for a higher Co. However, it has been verified that it can still result in an unstable model when dealing with more complex cases and hydrodynamics (e.g. wave-structure interaction, irregular waves, second order wave generation). The second option has also allowed to obtain results (previously shown in Figure 8) but again it has been noted that it does not suffice for many cases. Moreover, the first two options significantly increase the computational time. Therefore, a stabilisation based on filtering air velocity at the two-way coupled interfaces is proposed. The transfer of air-velocity can either be limited or stopped at the coupling interfaces. In this work, zero velocity at the air is applied. α = 0.5 is considered to detect the water-air interface. Basically, all boundary conditions are the same except the one for the velocity field for which the value of the variable at the interface (**U**) is multiplied by the volume fraction α. By doing so, the velocity at air is set to zero. Table 5 summarises the BCs used for stabilised the two-way model. Note that Table 6 shows which cases are run using the two-way

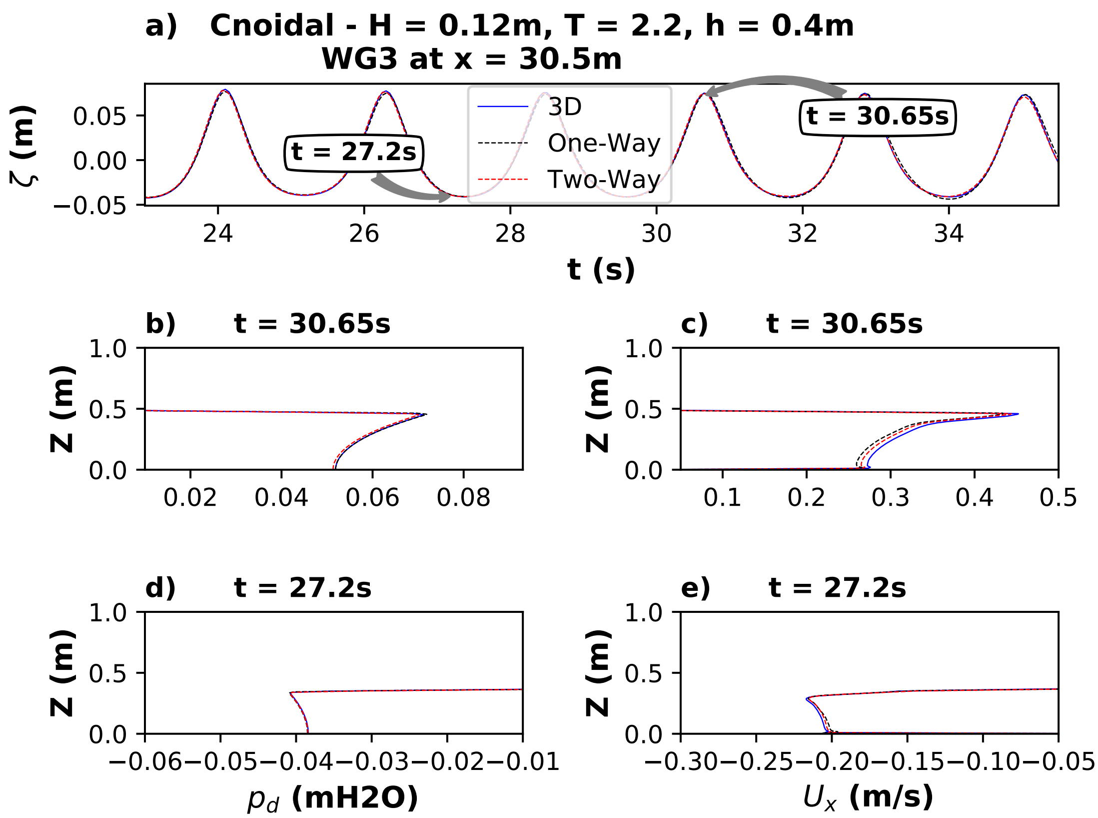

Figure 14: Simulation of Cnoidal waves: H = 0.12m, h = 0.4m, T = 2.2s. Panel a) shows the comparison of free surface elevation, b) and d) display the dynamic pressure (in meter of column water) and panels c) and e) show horizontal velocity profiles at WG3.

stabilised model.

It is worth to note that the imposition of zero velocity for the air-phase at the boundary of near-fields is not new but it has already been applied in past works. Particularly, when a single-phase model is coupled with a two-phase one, the air velocity is unknown as it is typically set to zero (Paulsen et al. (2014)) or in other cases the air solution is neglected (Biausser et al. (2004)). In the present work, it is important to check the mass conservation as the physics is artificially modified. To this aim, a simulation of an empty flume in two-way mode has been carried out. Waves are generated by moving boundary method and the outlet is defined as fully reflective. This setup guarantees that no mass inflows are associated to the wave generation and absorption. The aspect ratio is 4, the $Co = 0.3$ and the laminar model is used. A regular wave with $H = 0.05m$, $T = 1.5s$ and $h = 0.5m$ is generated and 180 seconds are simulated in order to check the mass conservation throughout a long simulation. The numerical model has been carried out in three modes:

1. two-way without stabilisation. BCs are as in Table 3
2. two-way with stabilisation applied on one-side only (3D side). BCs are as in Table 5 (for **U**

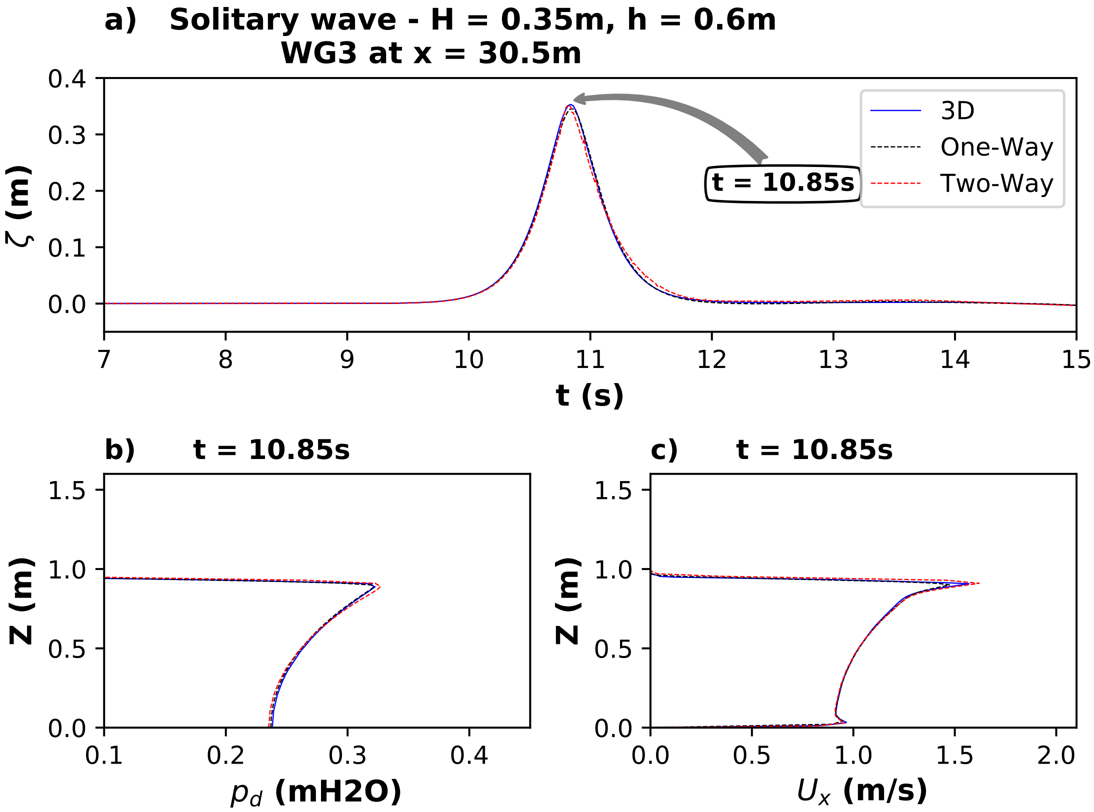

Figure 15: Simulation of a solitary wave: H = 0.35m, h = 0.6m. Panels a), b) and c) comparison of free surface elevation, dynamic pressure and horizontal velocity profiles, respectively at WG3.

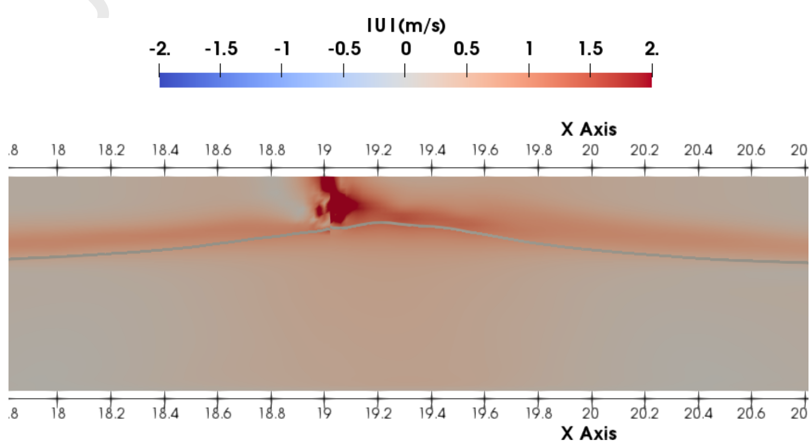

Figure 16: Two-way simulation: Fourth validation case (Stream Function wave). Spurious velocities in the air phase at the coupling boundaries ($x = 19.02m$) after the passage of a wave crest. The free surface is shown with a grey line. $Co = 0.3$.

Coupling directions	**BCs** Γ_{2D}	**BCs** Γ_{3D}
2D $\rightleftarrows$ 3D for α, p^*, k, ω	$\phi = \frac{1}{\lvert\mathbf{d}_p\rvert+\lvert\mathbf{d}_n\rvert}(\phi_p\lvert\mathbf{d}_n\rvert + \phi_n\lvert\mathbf{d}_p\rvert)$ $S_f\nabla\phi = \lvert\mathbf{S}_f\rvert\frac{\phi_n-\phi_p}{\lvert\mathbf{d}\rvert}\frac{\mathbf{S}_f\mathbf{d}}{\lvert\mathbf{S}_f\rvert\lvert\mathbf{d}\rvert}$	$\phi = \frac{1}{\lvert\mathbf{d}_p\rvert+\lvert\mathbf{d}_n\rvert}(\phi_p\lvert\mathbf{d}_n\rvert + \phi_n\lvert\mathbf{d}_p\rvert)$ $\mathbf{S}_f\nabla\phi = \lvert\mathbf{S}_f\rvert\frac{\phi_p-\phi_n}{\lvert\mathbf{d}\rvert}(-\frac{\mathbf{S}_f\mathbf{d}}{\lvert\mathbf{S}_f\rvert\lvert\mathbf{d}\rvert})$
for **U** two-sides stabilisation	$\phi = \frac{1}{\lvert\mathbf{d}_p\rvert+\lvert\mathbf{d}_n\rvert}(\phi_p\lvert\mathbf{d}_n\rvert + \phi_n\lvert\mathbf{d}_p\rvert)\cdot\alpha$ $S_f\nabla\phi = \lvert\mathbf{S}_f\rvert\frac{(\phi_n-\phi_p)\cdot\alpha}{\lvert\mathbf{d}\rvert}\frac{\mathbf{S}_f\mathbf{d}}{\lvert\mathbf{S}_f\rvert\lvert\mathbf{d}\rvert}$	$\phi = \frac{1}{\lvert\mathbf{d}_p\rvert+\lvert\mathbf{d}_n\rvert}(\phi_p\lvert\mathbf{d}_n\rvert + \phi_n\lvert\mathbf{d}_p\rvert)\cdot\alpha$ $\mathbf{S}_f\nabla\phi = \lvert\mathbf{S}_f\rvert\frac{(\phi_p-\phi_n)\cdot\alpha}{\lvert\mathbf{d}\rvert}(-\frac{\mathbf{S}_f\mathbf{d}}{\lvert\mathbf{S}_f\rvert\lvert\mathbf{d}\rvert})$
for **U** one-side stabilisation	$\phi = \frac{1}{\lvert\mathbf{d}_p\rvert+\lvert\mathbf{d}_n\rvert}(\phi_p\lvert\mathbf{d}_n\rvert + \phi_n\lvert\mathbf{d}_p\rvert)$ $S_f\nabla\phi = \lvert\mathbf{S}_f\rvert\frac{(\phi_n-\phi_p)\cdot\alpha}{\lvert\mathbf{d}\rvert}\frac{\mathbf{S}_f\mathbf{d}}{\lvert\mathbf{S}_f\rvert\lvert\mathbf{d}\rvert}$	$\phi = \frac{1}{\lvert\mathbf{d}_p\rvert+\lvert\mathbf{d}_n\rvert}(\phi_p\lvert\mathbf{d}_n\rvert + \phi_n\lvert\mathbf{d}_p\rvert)\cdot\alpha$ $\mathbf{S}_f\nabla\phi = \lvert\mathbf{S}_f\rvert\frac{(\phi_p-\phi_n)}{\lvert\mathbf{d}\rvert}(-\frac{\mathbf{S}_f\mathbf{d}}{\lvert\mathbf{S}_f\rvert\lvert\mathbf{d}\rvert})$

Table 5: Coupling directions and boundary conditions at the interface boundaries Γ_{2D} and Γ_{3D}: **Two-way** coupling with **stabilisation**. The generic variable (scalar or vector) is indicated with ϕ.

one-side stabilisation)

3. two-way with stabilisation applied on two-sides (2D-3D). BCs are as in Table 5 (for **U** two-sides stabilisation)

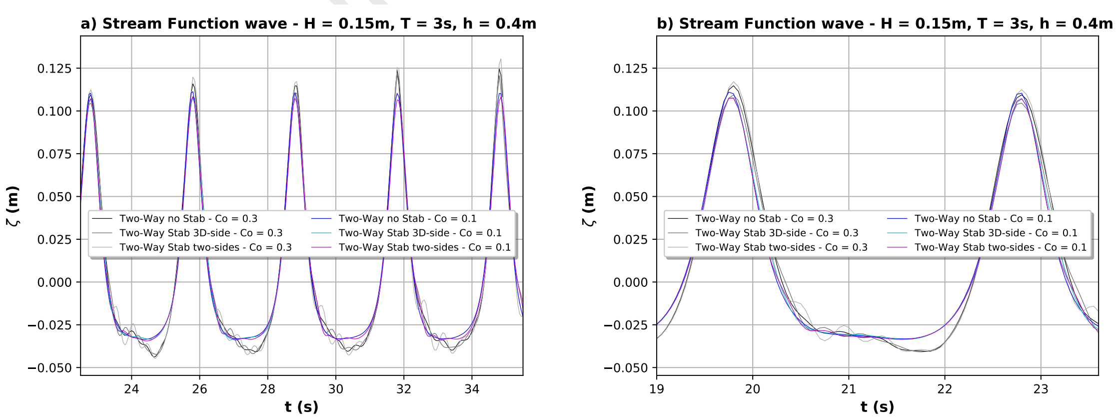

Figure 17: Stream Function two-way simulation: $H = 0.15$, $T = 3s$, $h = 0.4m$. Free surface comparison between the coupled models (un-stabilised and stabilised versions) and the 3D solution at WG2.

Figure 17 shows the results of free surface elevation for the two-way coupling schemes, comparing the stabilised models with the one without applying the stabilisation. Panel a) shows a group of five crests, while panel b) presents a time window between $t = 19s$ and $t = 23.5s$ in order to better appreciate the differences. It can be noted that for $Co = 0.3$ wave heights vary during the simulation time both for the stabilised and the un-stabilised cases. If no stabilisation is applied in this case the simulation becomes unstable and stops at $t = 34.9s$ (black line). When the stabilisation is applied, results are obtained although some differences with the un-stabilised solution are observed in the prediction of troughs. Particularly, when applying the stabilisation on two-sides (2D-3D), the irregularities in the troughs are more pronounced compared to the case where the stabilisation in applied on one-side only (3D side). However, it has to be note that by lowering the Courant number ($Co = 0.1$) the results improve significantly and the discrepancies among the stabilised and un-stabilised models become very small. The irregularity after the passage of wave troughs are strongly reduced and the estimation of the wave crests is satisfactory, although a very small decrease is shown for both stabilised models. The choice of a low Courant number, already shown in previous research (e.g. Larsen et al. (2019)) is crucial to get stable wave hydrodynamics, correct advection and accurate velocity fields beneath waves. It has been observed that for highly non-linear waves a high Co may lead to unstable solutions.

Results of the mass conservation are shown in Figure 18. Panel a) shows the global mass conservation error, which is calculated as the weighted average (over the cell volumes) of the continuity equation error for each time step. Panel b) displays the change of total mass in percentage throughout the simulation. From the inspection of panel a) it can be seen that the un-stabilised and the ”two-sides” stabilised models give close results in terms of mass conservation. The maximum error is comparable, i.e. $7.5 \cdot 10^{-5}$ and $8.1 \cdot 10^{-5}$, respectively. The initial mass of the system is also well conserved throughout the simulation (panel b). On the other hand, when the stabilisation is applied on one-side only (3D in this case), the mass conservation error increases with a maximum error of $\cdot 10^{-4}$ (panel a), and, consequently the mass of the system is decreased during the simulation (panel b). A possible cause is that the mass flow through one side (e.g. 3D) is different from the mass flow through the other side (e.g. 2D).

Note that in past research (i.e., Ferrer et al. (2016), the two-way coupled model was stabilised by forcing the solution of VOF equation to be bound between 0 and 1 a posteriori (after applying MULES algorithm). In the present research the VOF function is not altered artificially, as this may affect the correct detection of the free surface.

3.3 Sampling position for the one-way coupled models

All one-way simulations have been carried out using a fixed position of the sampling sensor. Although good results were obtained it has to be specified that the performance of the one-way coupling might be affected by the position of the sampling sensor. Particularly, understanding the influence of the active wave absorption at the outlet of the 2D domain on the positioning of the sampling sensor is essential in order to optimise the dimensions of the coupled domains. In general, the sampling sensor has to be placed at least 1.5 cells far from the outlet of the 2D regions. This is because the horizontal velocity profile at the adjacent cells (cell centres) of the 2D interface is constant as it is induced by the shallow water based active wave absorption. Such a uniform velocity profile cannot be used to transfer the hydrodynamics as it is not representative of the wave that approaches the coupled interfaces.

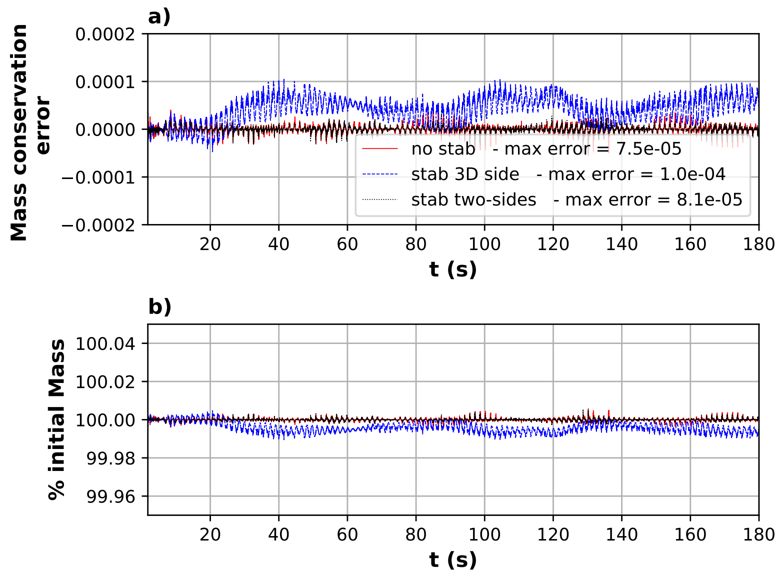

Figure 18: Mass conservation error. Panel a): weighted average (over the cell volumes) of the continuity equation error throughout the simulation. Panel b): change of the initial mass (%) throughout the simulation.

To test the effect of sampling position a simulation has been carried out with wave height $H = 0.12m$, wave period $T = 2.5s$ and a water depth $h = 1.1m$. The computational domain is the same as for the validation cases, but the height has been increased up to 1.6m. The aspect ratio is fixed to 1 ($\Delta_x = \Delta_y = \Delta_z = 0.01m$) and the Courant number is set to 0.1. Four positions of the sampling sensors have been tested: x_1 = 19.02m, x_2 = 19.8m, x_3 = 19.9m and x_4 = 19.985m. Note that x_4 corresponds to 1.5 cells far from the 2D outlet ($\Delta_x = 0.01m$). The four positions are chosen to consider sampling sensors close and far from the 2D outlet. Figure 19 shows the results of free surface elevation at WG3.

The main result that can be observed is that the by changing the position of the sampling sensor, the free surface elevation is not strongly affected. Very small deviations are observed among signals throughout the long simulation (panels from a to d of Figure 19). Wave heights do not vary significantly in time. Even when placing the sensor close to the absorbing boundary, the results are satisfactory. In particular, panel a shows that very small discrepancies are observed between the 3D results and the one-way simulations. It can also be observed that when placing the sampling sensor far from the coupling boundary (x_1), the free surface elevation is correctly predicted throughout the simulation time. The discrepancies slightly increase in time (panel b, c and d) and in particular for position x_4. The most evident discrepancy is shown in panel c, where a zoom at the wave crest (114.6s<t<115.2s) is shown. The maximum error is however below 7% in this case. In conclusion, as the position of the sampling gauge does not affect the results significantly, the sampling sensor can also be placed at 1.5 cells far from the outlet of the 2D domain (worst scenario). In Part II the performance of the one-way coupling will also be tested for wave-structure interaction, considering the worst scenario for the sampling position.

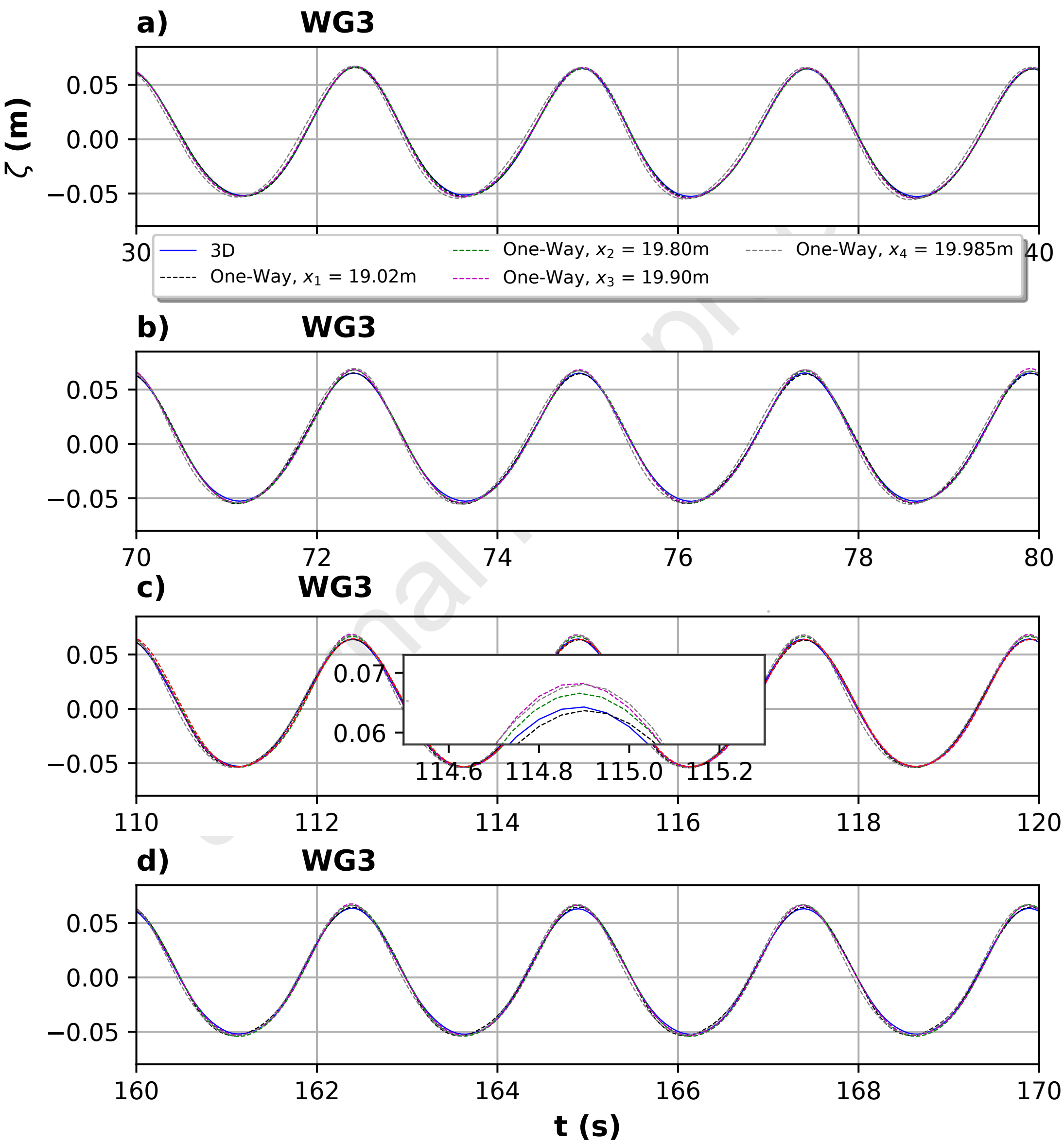

Figure 19: Free surface elevation comparison at WG3 between the one-way simulation and 3D solution. Four positions of the sampling sensors: x_1 = 19.02m, x_2 = 19.8m, x_3 = 19.9m and x_4 = 19.985m.

3.4 Error analysis

Next, an analysis of the relative error in estimating wave amplitudes has been carried out. The error is defined as follows:

$$\epsilon_{\%} = |1 - \frac{a_{coupled}}{a_{3D}}| \cdot 100$$

where $a_{coupled}$ is the wave amplitude of the coupled models (one-way or two-way) and a_{3D} is the one resulting from the 3D solution. On average, from the analysis of the free surface elevation (Figures 8 and 17) the maximum relative error ranges from 1% to 10%. The worst result is obtained for the Bichromatic wave in one-way mode, where the error slightly exceed 10% in the far field (panel b of Figure 10)., while in the majority of the cases the error remains below a 3%. These results are corroborated for free surface measurements at the coupling zone (Figures 8 and 17) as well as far from the coupling boundaries (Panels a of Figures 12, 13, 14 and 15).

As for the free surface, the relative error is analysed for the velocity profile and it reads as follows:

$$\epsilon_{\%} = |1 - \frac{U_x max_{coupled}}{U_x max_{3D}}| \cdot 100$$

where $U_x max_{coupled}$ is the maximum horizontal velocity from the coupled model and $U_x max_{3D}$ corresponds to the 3D simulation. The maximum error remains below 10%, throughout the cases simulated.

3.5 Field smoothness analysis

A relevant point of the present work is also the verification of smoothness of the free surface, velocity and pressure fields. This is of key importance to ensure that no information is lost throughout the simulations. Indeed, if the profiles are not perfectly smooth some information is lost at each time step, which results in a high decrease or increase of the flow variable (pressure, velocity, free surface, etc.). Figure 20 illustrates the dynamic pressure and velocity at the coupling interface for the one-way simulation of a Stokes II wave ($H = 0.1m$, $T = 2.5s$ and $h = 0.6m$). In particular free surface is depicted with red and green lines for the 2D and 3D regions, respectively. The coupling interfaces are located between the red and green lines. It can be observed that both pressure and velocity profiles (panel a and b, respectively) are quite smooth all along the water depth (z-axis) with no discontinuities. Similar results are obtained for the two-way simulation (Figure 21). A solitary wave simulation has been carried out (case 1 of the validation), in which the wave propagates from the 2D to the 3D domain, and gets reflected to the outlet of the 3D domain travelling back from the 3D to 2D region. A fully reflective boundary is defined at the outlet of the 3D region (100% reflection). The first two snapshots (panels a and b) refer to the wave propagation forward (2D to 3D). The crest maximum is displayed at the interface location. Again, the profiles are smooth and no discontinuities are shown. Identical results are also illustrated for the wave propagation from 3D to 2D (panel c). A smooth profile is shown for the dynamic pressure both when wave travels from 2D to 3D and vice versa.

Another fully reflective simulation has been carried out increasing the wave height. Here, a solitary wave with wave height $H = 0.2m$ and water depth $h = 0.5m$ is generated. Figure 22 shows the comparison between 3D, one-way and two-way simulations when the wave propagates along the positive ($t = 8.65s$) and negative ($t = 24.35s$) x-direction. The small vertical lines at $x = 19.02m$ indicate the position of the coupled interfaces for the coupled models. The first result is that both coupled models perform similar when transferring the wave from 2D to 3D (panels a, b and c) ($t = 8.65s$) and the velocity field appears to be smooth (panels a, b and c). At $t = 24.15s$, it can be noted that while in the one-way model the 3D interface start absorbing the wave (panel f), in the two-way approach the wave is transferred from 3D to 2D (panel d). From the inspection of the two-way results (panel d) it can be observed that the velocity field is similar to the full 3D (panel e). Again, the velocity field appears to be smooth at the two-way coupled interfaces (panel e).

One last case considering full reflection at the outlet of the 3D domain is carried out with regular waves (N = 11 in Table 4), but it is not shown here for a sake of synthesis. However, results of the performance in terms of computational time will be shown in the following for the reflective cases carried out both in 3D and coupled modes (N=10 and N=11 in Table 4).

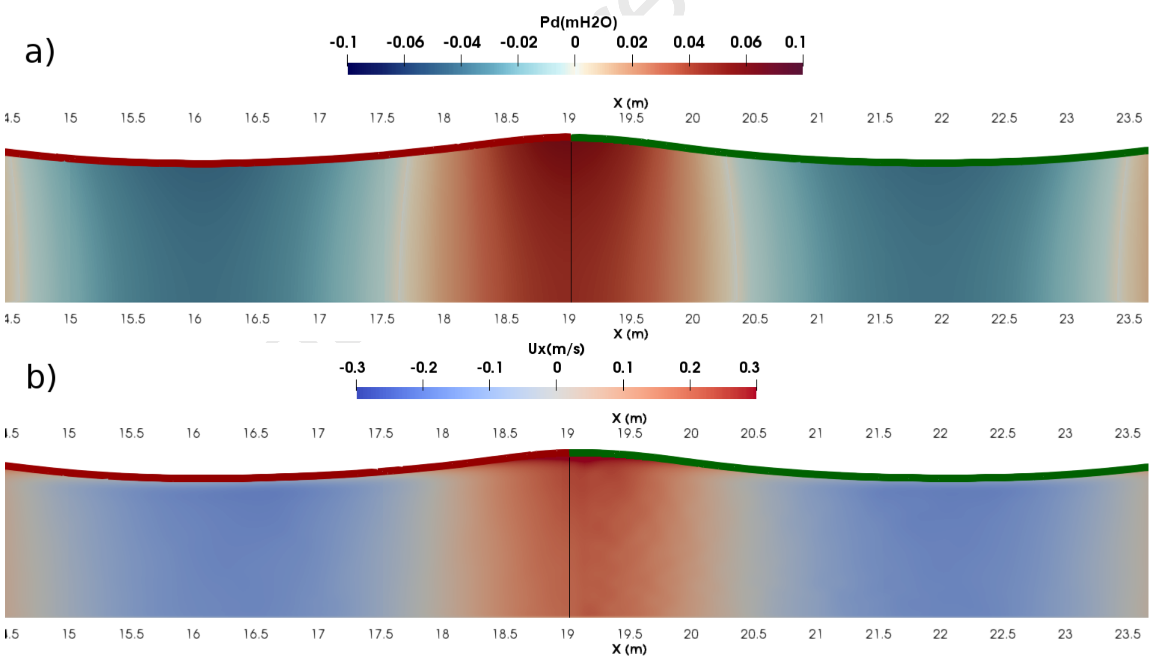

Figure 20: One-way simulation of a Stokes II wave ($H = 0.1m, T = 2.5s, h = 0.6m$) propagating in an empty fully reflective numerical domain (100 % reflection at the outlet of the 3D region). Case 3 in Table 4. Dynamic pressure in m of water column (mH2O). Black lines indicate the coupling boundary.

Finally, a simulation of a long regular wave series considering the propagation of a cnoidal-type wave with wave height $H = 0.15m$, wave period $T = 4s$ and water depth $h = 0.4m$ has been developed to show how the velocity profile is affected by the shallow water wave absorption. Figure 23 (one-way mode) shows the free surface elevation and horizontal velocity obtained from the propagation of the Cnoidal wave in an empty numerical domain as in Figure 7. As anticipated, very smooth profiles are obtained when the the first wave is transferred from the 2D to the 3D domain (Figure 23 from panel a) to panel d)). The effect of the active wave absorption at the outlet of the 2D region and at the inlet of the 3D domain slightly alters the wave profile, as can be clearly seen in the bottom panel of Figure 23 ($t = 108.8s$ and $t = 109s$). The effect of a uniform velocity correction along the water depth is to produce evanescent modes as can be observed in panel e) and f) of Figure 23. However, it should be noted that the wave hydrodynamics is not significantly altered. Although, it may occur that evanescent modes are generated at the coupled interfaces due to the active absorption, it has been previously shown (Figure 19) that the active wave absorption does not affect significantly the shape of the waves, neither close nor far from the coupled interfaces. Figure 24 shows the comparisons between the coupled (both one-way and two-way) and the full simulations for the cnoidal wave case shown in Figure 23. Here, a good correlation between the coupled (one-way and two-way) and 3D results is found at the coupling interface (panels a, b and c). The one-way model slightly differs from the 3D model due to the active wave absorption correction. However the velocity profile is comparable to the 3D one, as well as the wave shape. The two-way model (panel c) remains more in line with the 3D results although the velocity beneath the crest is slightly higher. Both coupled model show a very good correspondence with the 3D solution far from the coupling location (panels d, e and f). Wave crests are correctly predicted as well as the velocity beneath the crest, and no phase lags are observed. In Part II, it will also be shown as the one-way coupling works well for long time simulations of wave and structure interaction and allows to predict forces on structure with an acceptable accuracy. It is worth mentioning that the two-way model allows to avoid the reflection problem thanks to the nature of the BCs presented in Section 3, as waves are free to travel through the interfaces.

In general, it has been shown that both one-way and two-way algorithms work well. Both one-way and two-way couplings lead to accurate results for free surface, velocity and pressure fields close and far from the coupled interfaces, and small deviation from the 3D solutions are observed. However, the two-way coupling may suffer from instabilities due to high air-velocities at the interfaces when dealing with extreme hydrodynamics. For this reason, a stabilised two-way algorithm which allows obtaining highly accurate results with an increased stability and robustness has also been proposed. The one-way methodology can give accurate results with a small influence on the sampling sensor position also when long duration of wave series are considered. The active wave absorption may introduce evanescent modes. However, as shown, the one-way model give stable wave patterns in the far field, comparable to the 3D solution and the two-way simulations.

4 Discussion

One of the most significant findings emerging from this study is that wave generation, transformation and interaction with structures in large domains can be efficiently simulated with CFD models using 2D-3D couplings, resulting in a very high accuracy and affordable computational cost and avoiding the assumption of lower models (e.g. potential models). It is worth to notice that a two-way coupling is also introduced for the first time to 2D-3D RANS-RANS coupled models compared to similar couplings (El Safti et al. (2014)). Indeed, El Safti et al. (2014) performed

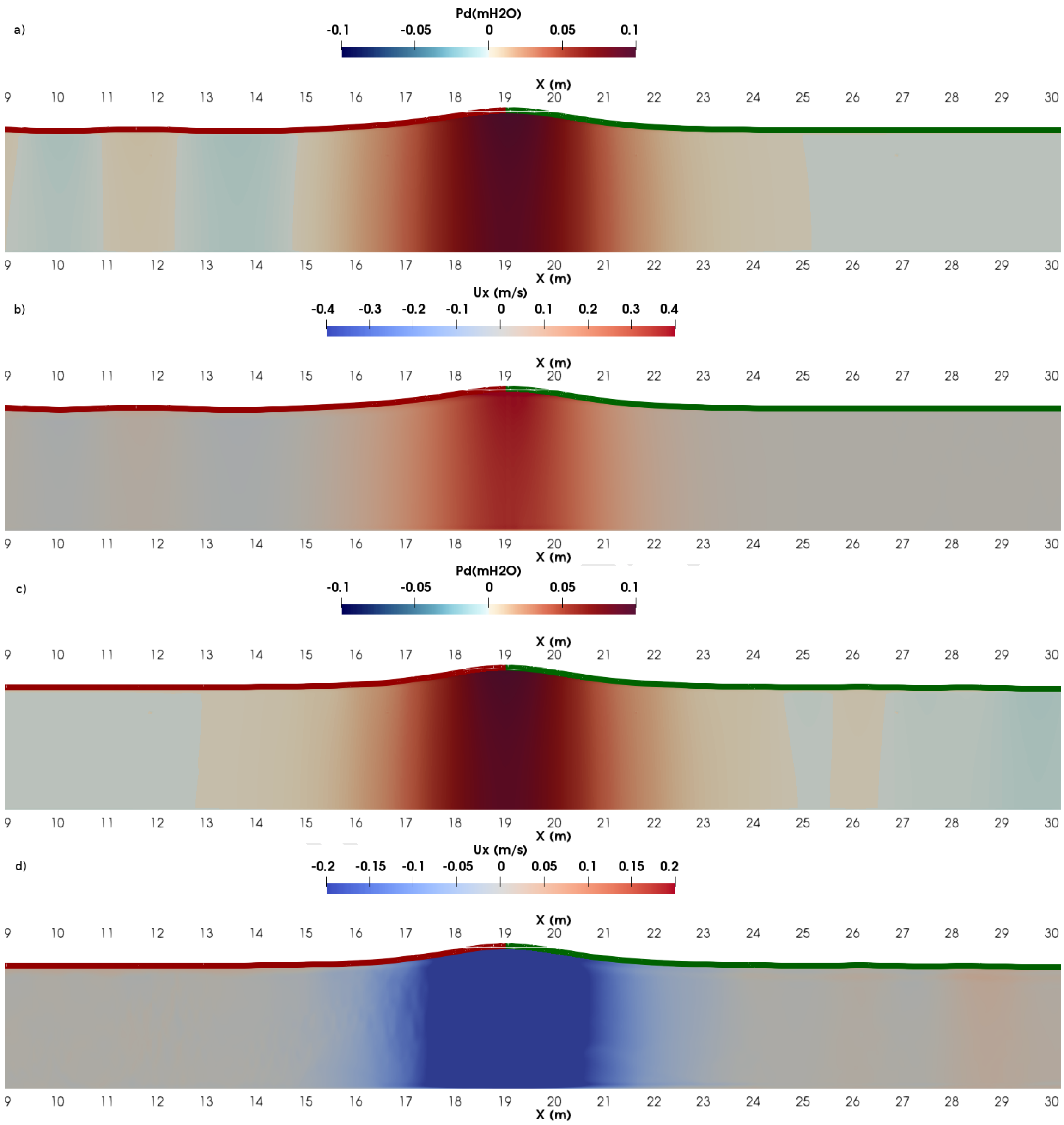

Figure 21: Two-way simulation of a solitary wave propagating in an empty fully reflective numerical domain . Case 1 in Table 4 but with fully reflective wall at the outlet of the 3D domain. Horizontal velocity (panels b and d) in m/s. Dynamic pressure (panels a and c) in m of water column (mH2O).

one-way simulations using post-processed sensors from 2D RANS models and used them as input for the 3D RANS solver. The model proposed in this work results to be more efficient than the above research given that: (i) it does not use relaxation zones at the interfaces thus not increasing the computational domain (ii) wave information is transferred including first and second order components without applying any relaxation functions that replace the calculated hydrodynam-

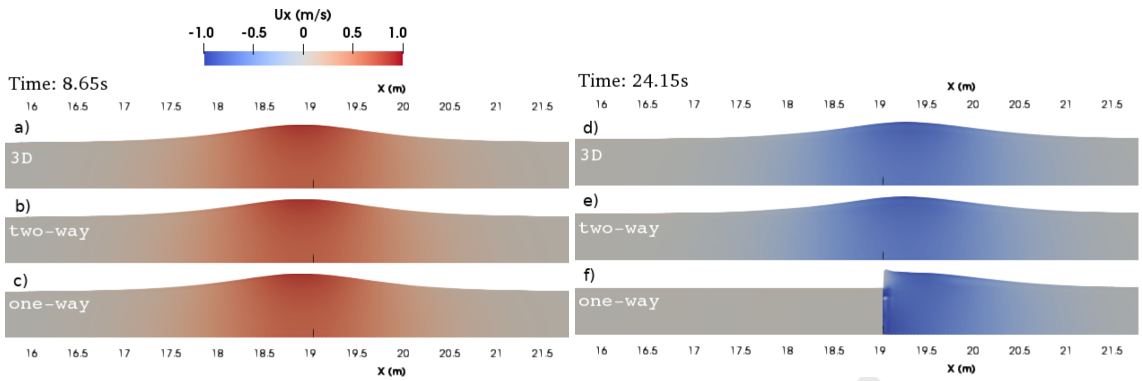

Figure 22: Comparison of the horizontal velocity field for the one-way, two-way and 3D simulations. The vertical black lines at x = 19.02m indicate the position of the coupled interfaces. Fully reflective case of solitary wave, N = 10 in Table 4. Panels a), b) and c) show the passage of the wave crest from 2D to 3D domain. Panels d), e) and f) display the passage of the wave crest from 3D to 2D region.

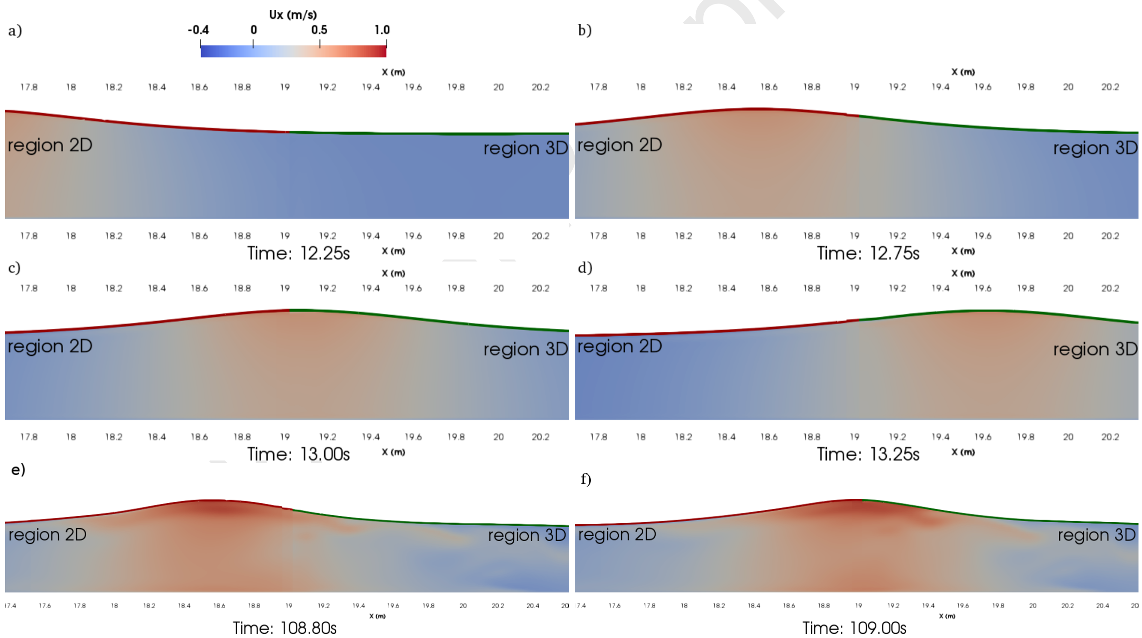

Figure 23: Cnoidal wave propagation in an empty numerical domain. H = 0.15, h = 0.4m, T = 4s. The 2D/3D interface is located at x=19.02m. The velocity field is shown in the panels at six instants of time.

ics (ii) it also provides the two-way coupling scheme for those cases where the bi-directionality of the flows plays a role.

We remark that the computational cost for practical applications requiring high mesh refinement will always be governed by the 3D computational domain whereas the computational time of the 2D region can be one-order of magnitude lower than the 3D one. The larger the domain the greater is the difference in the computational time between 2D and 3D models. This aspect reinforces the motivation of the proposed implementations in this work, above all when studying

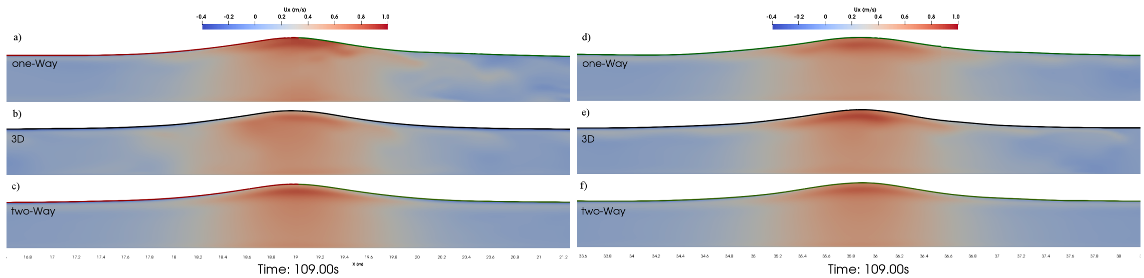

Figure 24: Cnoidal wave propagation in an empty numerical domain. H = 0.15, h = 0.4m, T = 4s. The 2D/3D interface is located at x=19.02m. Comparison of the velocity field for the one-way, two-way and 3D simulations. The velocity field is shown at the coupling zone (panels a, b and c) and far from the coupling zone (panels d, e and f).

large scale problems for correctly generating and transforming wave hydrodynamics.

The implementation proposed here is applicable for practical cases where the three-dimensional effects are important (confined) in the near-field. By all means, the hypothesis that the 3D effects are confined in the near field must be acceptable.

The present work showed that the coupling models are capable of transferring information producing a good match with the 3D simulations. The two-way model was also stabilised as shown in the paper by avoiding the transfer of the air velocity at the coupled interfaces (on one or two-sides). Alternatively, the precision of the strong coupling may be improved by setting a threshold value to the air velocity at the interface. However, it is beyond the scope of this research to find the optimal stabilisation approach, but it will be studied in detail in future work. Note that the appearance of the high velocities at the water-air interface is not new, since it was already found in past research (El Safti et al. (2014)). Indeed, El Safti et al. (2014) stated that the introduction of a short relaxation (overlapping) zone to perform a one-way 2D-3D coupling may cause the development of very high artificial fluid velocities, especially at the water-air interface. However, in the present work the one-way coupling, based on the active wave absorption and non-overlapping scheme, does not induce any spurious additional velocity to the fluids.

The CPU time saving represents an important goal achieved in the present research. The ratio of computational acceleration (n_{speed}) and the computation load saved (%) are calculated as follows:

$$n_{speed} = \frac{CPU_{3D}}{CPU_{coupled}} \qquad \% = (1 - \frac{CPU_{coupled}}{CPU_{3D}}) \cdot 100$$

where CPU_{3D} is the execution time of the 3D simulation and $CPU_{coupled}$ is the computational time of the coupled model (one-way or two-way). The simulations are performed using a computer desktop with the following characteristics: Intel(R) Core(TM) i7-7700K CPU 4.20GHz CPU unit, 32GB RAM. Runs have been parallelised using 8 processor units. Results of computational time are summarised in Table 6. The main conclusion is that the coupled models allow to speed-up the simulations by a factor in the range of 1.2 and 5, approximately. The speed-up is strongly dependent on the hydrodynamics simulated. Such as, in the presence of full reflected regular waves the coupled models can result less efficient (speed-up between 1.2 and 1.5). Moreover, for fully

Case	CPU_{3D} (h)	CPU_{1way} (h)	CPU_{2way} (h)	n_{speed} $_{3D-1way}$	n_{speed} $_{3D-2way}$	% $_{3D-1way}$	% $_{3D-2way}$	time (s)	Co	two-way stab
N = 1	6.4	4.2	3.8	1.68	1.52	34	41	40	0.1	-
N = 2	8.91	4.5	4.15	1.98	2.14	49	53	40	0.1	-
N = 3	17.5	9.79	8.3	1.78	2.11	44	53	40	0.1	-
N = 4	23.16	16.9	12.7	1.37	1.82	27	54	40	0.1	active
N = 5	42.78	24.87	23.4	1.72	1.83	42	45	17	0.3	-
N = 6	32.07	16.37	17.4	1.96	1.88	49	46	40	0.1	-
N = 7	280.68	167.5	158.8	1.68	1.77	40	43	120	0.1	-
N = 8	133.33	62.3	55.7	2.14	2.39	53	58	200	0.1	-
N = 9	56.3	29.3	26.7	1.92	2.11	48	53	200	0.3	-
N = 10	50	10	37	5	1.35	80	26	55	0.1	-
N = 11	233	149.7	194.4	1.56	1.2	35.8	16.6	120	0.1	-

Table 6: Computational speed-up obtained for the cases simulated. All the cases have been simulated with 8 processor units (8 procs) Intel(R) Core(TM) i7-7700K CPU 4.20GHz. $\mathbf{CPU}_{3D}$, $\mathbf{CPU}_{1way}$ and $\mathbf{CPU}_{2way}$ are the computational times for the 3D, one-way and two-way simulations, respectively. The computational acceleration ($\mathbf{n}_{speed}$) and load saved (%) are reported. **N** refers to the number of case in Table .

reflective cases the one-way is more efficient that the two-way coupling, for the rest of the cases analysed (non reflective), the one-way coupling resulted as the slightly less time-saving. It should be noted that the validation cases are ideal case in which the 3D domain is as large as the 2D one, while for practical cases the 3D domain will be generally shorter than the 2D region, thus leading to a significant reduction of the computational time. Moreover, the simulations can be further accelerated by pushing the coupling interfaces as close as possible to the near field. This can be better achieved in a RANS-RANS approach than for lower coupling model (e.g. BT-RANS).

5 Concluding remarks

Modelling coastal processes using CFD software is a challenging task, mainly due to its extremely expensive computational time when simulating large three dimensional domains. to reduce the computational time and to avoid potential flow assumptions, 2D-3D weak and strong RANS-RANS couplings were proposed in this paper to form the basis for an efficient high fidelity coupling methodology for first and second order hydrodynamics.

The first conclusion is that, compared to 3D models, the one-way and two-way couplings are very accurate for transferring a wide range of hydrodynamics, considering non-linear waves, and second order wave generation including the bound-long wave mechanisms. The couplings can be used to solve wave hydrodynamics from the far to the near field for typical problems in coastal engineering. Furthermore, the work presented here does not increase the computational domain compared to an existing 2D-3D CFD coupled model found in the literature, as neither relaxation zones for absorbing waves nor overlapping are needed at the coupling interfaces (El Safti et al.

(2014)). Compared to past research (El Safti et al. (2014)), the present work also introduced the two-way coupling scheme to study bi-directional flows. Results showed that in general the strong coupling is more accurate than the weak one, although it is slightly less robust. The two-way coupling appears to give results better correlated with the 3D solution than the one-way approaches, although under extreme wave loads a stabilised solution may be needed, as proposed in Section 3.2. The two-way model is thus very stable without additional numerics, such as, bounding the solution of the VOF indicator function as found in past works (Ferrer et al. (2016)). The applicability of the one-way model can overcome the limitations of the 2D flow at the coupled interfaces. In a practical way, the proposed method may be used for highly 3D and reflective flows which induce 3D flow at the coupling interfaces. The three-dimensional waves reflected from 3D to 2D can be absorbed by a one-way type BC by using a multi-paddle absorbing boundary. In this case, the one-way coupled model should be used with caution, verifying that the 3D interface is working as a 3D wave-maker for generating and absorbing waves.

Based on the outcome of this work, it can be concluded that the couplings can be highly accurate and quite stable in transferring a wide range of wave hydrodynamics, also when the bi-directionality of the flow plays a role (two-way), and with the benefit of reducing the computational time, especially for cases where three-dimensionality flows are dominant in the near field.

Nomenclature

BEM Boundary Element Method

BT Boussinesq Type Equations

CFD Compuational fluid dynamics

FEM Finite Element Method

FNPF Fully Non-Linear Potential Flow

FVM Finite Volume Method

NLSW Non-Linear Shallow Water Equations

NS Navier-Stokes Equations

RANS Reynolds Averaged Navier-Stokes Equations

SWE Shallow Water Equations

VARANS Volume Averaged Reynolds Averaged Navier-Stokes Equations

WSI Wave structure interaction

Bibliography

Altomare, C., Suzuki, T., Dominguez, J., Crespo, A., 2014. Coupling between SWASH and SPH for real coastal problems, in: 9th International Spheric workshop, pp. 1–6.

Berberović, E., van Hinsberg, N.P., Jakirlić, S., Roisman, I.V., Tropea, C., 2009. Drop impact onto a liquid layer of finite thickness: Dynamics of the cavity evolution. Physical Review E 79, 036306.

Biausser, B., Fraunié, P., Grilli, S.T., Marcer, R., et al., 2004. Numerical analysis of the internal kinematics and dynamics of 3-D breaking waves on slopes. International Journal of Offshore and Polar Engineering 14.

Brackbill, J.U., Kothe, D.B., Zemach, C., 1992. A continuum method for modeling surface tension. Journal of computational physics 100, 335–354.

Brocchini, M., 2013. A reasoned overview on Boussinesq-type models: the interplay between physics, mathematics and numerics. Proceedings of the Royal Society A: Mathematical, Physical and Engineering Sciences 469, 20130496.

Colicchio, G., Greco, M., Faltinsen, O., 2006. A BEM-level set domain-decomposition strategy for non-linear and fragmented interfacial flows. International journal for numerical methods in engineering 67, 1385–1419.

Devolder, B., Rauwoens, P., Troch, P., 2017. Application of a buoyancy-modified k-ω sst turbulence model to simulate wave run-up around a monopile subjected to regular waves using openfoam®. Coastal Engineering 125, 81–94.

Di Paolo, B., Lara, J.L., Barajas, G., Losada, I.J., a. Waves and structure interaction using multi-domain couplings for Navier-Stokes solvers in OpenFOAM ®. Part I: Implementation and validation (referred to as Part 1). Coastal Engineering .

Di Paolo, B., Lara, J.L., Barajas, G., Losada, I.J., b. Waves and structure interaction using multi-domain couplings for Navier-Stokes solvers in OpenFOAM ®. Part II: Application (referred to as Part 2). Coastal Engineering .

Duz, B., Bunnik, T., Kapsenberg, G., 2016. Numerical simulation of nonlinear free surface water waves using a coupled potential flow-URANS/VOF approach. ECCOMAS Congress 2016 VII European Congress on Computational Methods in Applied Sciences and Engineering .

El Safti, H., Bonakdar, L., Oumeraci, H., 2014. A hybrid 2D-3D CFD model system for offshore pile groups subject to wave loading. ASME 2014 33rd International Conference on Ocean, Offshore and Arctic Engineering .

Ferrer, P.M., Causon, D., Qian, L., Mingham, C., Ma, Z., 2016. A multi-region coupling scheme for compressible and incompressible flow solvers for two-phase flow in a numerical wave tank. Computers & Fluids 125, 116–129.

Fourtakas, G., Stansby, P.K., Rogers, B.D., Lind, S.J., Yan, S., Ma, Q., et al., 2018. On the coupling of incompressible SPH with a finite element potential flow solver for nonlinear free-surface flows. International Journal of Offshore and Polar Engineering 28, 248–254.

Guo, L.d., Sun, D.p., Hao, W., 2012. A new numerical wave flume combining the 0–1 type bem and the vof method. Journal of Hydrodynamics, Ser. B 24, 506–517.

Higuera, P., Lara, J.L., Losada, I.J., 2013a. Realistic wave generation and active wave absorption for Navier-Stokes models: Application to OpenFOAM®. Coastal Engineering 71, 102–118.

Higuera, P., Lara, J.L., Losada, I.J., 2013b. Simulating coastal engineering processes with openfoam®. Coastal Engineering 71, 119–134.

Higuera, P., Lara, J.L., Losada, I.J., 2014a. Three-dimensional interaction of waves and porous coastal structures using openfoam®. part i: Formulation and validation. Coastal Engineering 83, 243–258.

Higuera, P., Lara, J.L., Losada, I.J., 2014b. Three-dimensional interaction of waves and porous coastal structures using openfoam®. part ii: Application. Coastal Engineering 83, 259–270.

Higuera, P., Losada, I.J., Lara, J.L., 2015. Three-dimensional numerical wave generation with moving boundaries. Coastal Engineering 101, 35–47.

Hildebrandt, A., Sriram, V., Schlurmann, T., et al., 2013. Simulation of focusing waves and local line forces due to wave impacts on a tripod structure, in: The Twenty-third International Offshore and Polar Engineering Conference, International Society of Offshore and Polar Engineers.

Issa, R.I., 1986. Solution of the implicitly discretised fluid flow equations by operator-splitting. Journal of computational physics 62, 40–65.

Jacobsen, N.G., Fuhrman, D.R., Fredsøe, J., 2012. A wave generation toolbox for the open-source CFD library: OpenFoam®. International Journal for numerical methods in fluids 70, 1073–1088.

Janssen, C.F., Krafczyk, M., Grilli, S., et al., 2010. Modeling of wave breaking andwave-structure interactions by coupling of fully nonlinear potential flow and lattice-boltzmann models, in: The Twentieth International Offshore and Polar Engineering Conference, International Society of Offshore and Polar Engineers.

Kassiotis, C., Ferrand, M., Violeau, D., Rogers, B., Stansby, P., Benoit, M., 2011. Coupling SPH with a 1-D Boussinesq-type wave model, in: 6th International SPHERIC Workshop, pp. 241–247.

Kemper, J., Windt, C., Graf, K., Ringwood, J.V., 2019. Development towards a nested hydrodynamic model for the numerical analysis of ocean wave energy systems .

Kim, S.H., Yamashiro, M., Yoshida, A., 2010. A simple two-way coupling method of BEM and VOF model for random wave calculations. Coastal Engineering 57, 1018–1028.

Kumar, P., Yang, Q., Jones, V., McCue-Weil, L., 2015. Coupled SPH-FVM simulation within the OpenFOAM framework. Procedia Iutam 18, 76–84.

Lachaume, C., Biausser, B., Fraunié, P., Grilli, S.T., Guignard, S., et al., 2003. Modeling of breaking and post-breakingwaves on slopes by coupling of BEM and VOF methods, in: The Thirteenth International Offshore and Polar Engineering Conference, International Society of Offshore and Polar Engineers.

Lara, J., Ruju, A., Losada, I., 2011a. Reynolds Averaged Navier-Stokes modelling of long waves induced by a transient wave group on a beach. Proceedings of the Royal Society A: Mathematical, Physical and Engineering Sciences 467, 1215–1242.

Lara, J.L., Ruju, A., Losada, I.J., 2011b. Reynolds Averaged Navier-Stokes modelling of long waves induced by a transient wave group on a beach, in: Proceedings of the Royal Society of London A: Mathematical, Physical and Engineering Sciences, The Royal Society. pp. 1215–1242.

Larsen, B.E., Fuhrman, D.R., 2018. On the over-production of turbulence beneath surface waves in Reynolds Averaged Navier-Stokes models. Journal of Fluid Mechanics 853, 419–460.

Larsen, B.E., Fuhrman, D.R., Roenby, J., 2019. Performance of interFoam on the simulation of progressive waves. Coastal Engineering Journal 61, 380–400.

Li, Y., 2016. Implementation of multiple time steps for the multi-physics solver based on chtMultiRegionFoam. Proceedings of CFD with OpenSource Software, 2016, Edited by Nilsson H. .

Li, Z., Bouscasse, B., Ducrozet, G., Gentaz, L., Touzé, D.L., Ferrant, P., 2020. Spectral wave explicit navier-stokes equations for wave-structure interactions using two-phase computational fluid dynamics solvers. arXiv preprint arXiv:2005.12716 .

Longuet-Higgins, M.S., Stewart, R., 1962. Radiation stress and mass transport in gravity waves, with application to 'surf beats'. Journal of Fluid Mechanics 13, 481–504.

Lu, X., Chandar, D.D.J., Chen, Y., Lou, J., 2017. An overlapping domain decomposition based near-far field coupling method for wave structure interaction simulations. Coastal Engineering 126, 37–50.

Mintgen, F., Manhart, M., 2018. A bi-directional coupling of 2D shallow water and 3D Reynolds-Averaged Navier-Stokes models. Journal of Hydraulic Research 56, 771–785.

Narayanaswamy, M.S., 2008. A hybrid Boussinesq-SPH wave propagation model with applications to forced waves in rectangular tanks. Ph.D. thesis. Johns Hopkins University.

Patankar, S.V., Spalding, D.B., 1983. A calculation procedure for heat, mass and momentum transfer in three-dimensional parabolic flows, in: Numerical Prediction of Flow, Heat Transfer, Turbulence and Combustion. Elsevier, pp. 54–73.

Paulsen, B.T., Bredmose, H., Bingham, H.B., 2014. An efficient domain decomposition strategy for wave loads on surface piercing circular cylinders. Coastal Engineering 86, 57–76.

Quarteroni, A., Valli, A., 1999. Domain decomposition methods for partial differential equations. BOOK, Oxford University Press.

Rusche, H., 2003. Computational fluid dynamics of dispersed two-phase flows at high phase fractions (doctoral dissertation, imperial college london. University of London .

Schäffer, H.A., Steenberg, C.M., 2003. Second-order wavemaker theory for multidirectional waves. Ocean Engineering 30, 1203–1231.

Simonetti, I., Cappietti, L., Elsafti, H., Oumeraci, H., 2018. Evaluation of air compressibility effects on the performance of fixed owc wave energy converters using cfd modelling. Renewable energy 119, 741–753.

Sitanggang, K., Lynett, P., 2010. Multi-scale simulation with a hybrid Boussinesq-RANS hydrodynamic model. International Journal for Numerical Methods in Fluids 62, 1013–1046.

Sitanggang, K.I., 2008. Boussinesq-Equation and RANS hybrid wave model. volume 69.

Sitanggang, K.I., Lynett, P.J., Liu, P.L.F., 2007. Development of a Boussinesq-RANS VOF hybrid wave model, in: Coastal Engineering 2006: (In 5 Volumes). World Scientific, pp. 24–35.

Sriram, V., Ma, Q., Schlurmann, T., 2014. A hybrid method for modelling two dimensional non-breaking and breaking waves. Journal of computational physics 272, 429–454.

Vandebeek, I., Gruwez, V., Altomare, C., Suzuki, T., Vanneste, D., De Roo, S., Toorman, E., Troch, P., 2018. Towards an efficient and highly accurate coupled numerical modelling approach for wave interactions with a dike on a very shallow foreshore, in: Coastlab 2018, pp. 1–10.

Verbrugghe, T., Domínguez, J.M., Crespo, A.J., Altomare, C., Stratigaki, V., Troch, P., Kortenhaus, A., 2018. Coupling methodology for Smoothed Particle Hydrodynamics modelling of non-linear wave-structure interactions. Coastal Engineering 138, 184–198.

Verbrugghe, T., Stratigaki, V., Altomare, C., Domínguez, J., Troch, P., Kortenhaus, A., 2019. Implementation of open boundaries within a two-way coupled SPH model to simulate nonlinear wave–structure interactions. Energies 12, 697.

Vreugdenhil, C.B., 2013. Numerical methods for shallow-water flow. volume 13. Springer Science & Business Media.

Vukčević, V., Jasak, H., Malenica, Š., 2016. Decomposition model for naval hydrodynamic applications, part i: Computational method. Ocean Engineering 121, 37–46.

Zhang, Y., Peszynska, M., Yim, S., 2013. Coupling of viscous and potential flow models with free surface for near and far field wave propagation. International Journal of Numerical Analysis and Modeling 4, 256–282.

Highlights

- One-way and two-way 2D-3D multi-domain couplings have been developed for Navier-Stokes models
- A wide range of wave conditions were successfully transferred, including infragravity waves
- A high field smoothness was shown through the interfaces
- The 2D-3D approach has proven to be robust and stable
- The methodology significantly reduces the computational time

AUTHORSHIP STATEMENT

Manuscript title: **Wave and structure interaction using multi-domain couplings for Navier-Stokes solvers in OpenFOAM. Part I: Implementation and validation**

All persons who meet authorship criteria are listed as authors, and all authors certify that they have participated sufficiently in the work to take public responsibility for the content, including participation in the concept, design, analysis, writing, or revision of the manuscript. Furthermore, each author certifies that this material or similar material has not been and will not be submitted to or published in any other publication before its appearance in the *Coastal Engineering*.

Authorship contributions

Please indicate the specific contributions made by each author (list the authors' initials followed by their surnames, e.g., Y.L. Cheung). The name of each author must appear at least once in each of the three categories below.

Category 1

Conception and design of study: B. Di Paolo, J.L. Lara, G. Barajas, I.J. Losada
Investigation: B. Di Paolo, J.L. Lara, G. Barajas
Formal analysis: B. Di Paolo, J.L. Lara, G. Barajas.

Category 2

Drafting the manuscript: B. Di Paolo, J.L. Lara
Revising the manuscript critically for important intellectual content: B. Di Paolo, J.L. Lara, G. Barajas, I.J. Losada

Category 3

Approval of the version of the manuscript to be published (the names of all authors must be listed): B. Di Paolo, J.L. Lara, G. Barajas, I.J. Losada.

Acknowledgements

All persons who have made substantial contributions to the work reported in the manuscript (e.g., technical help, writing and editing assistance, general support), but who do not meet the criteria for authorship, are named in the Acknowledgements and have given us their written permission to be named. If we have not included an Acknowledgements, then that indicates that we have not received substantial contributions from non-authors.

This statement is signed by all the authors (*a photocopy of this form may be used if there are more than 10 authors***):**

Author's name (typed)	Author's signature	Date
B. Di Paolo		September 30th 2020
J.L.Lara		September 30th 2020
G. Barajas		September 30th 2020
I.J.Losada		September 30th 2020

Declaration of interests

☒ The authors declare that they have no known competing financial interests or personal relationships that could have appeared to influence the work reported in this paper.

☐The authors declare the following financial interests/personal relationships which may be considered as potential competing interests: